

THESIS

ON THE OBSERVED RELATIONSHIPS BETWEEN VARIABILITY IN SEA SURFACE
TEMPERATURES AND THE ATMOSPHERIC CIRCULATION IN THE NORTHERN
HEMISPHERE

Submitted by

Samantha M. Wills

Department of Atmospheric Science

In partial fulfillment of the requirements

For the Degree of Master of Science

Colorado State University

Fort Collins, Colorado

Fall 2015

Master's Committee:

Advisor: David W. J. Thompson

Elizabeth Barnes

Subhas Karan Venayagamoorthy

Copyright by Samantha M. Wills 2015

All Rights Reserved

ABSTRACT

ON THE OBSERVED RELATIONSHIPS BETWEEN VARIABILITY IN SEA SURFACE TEMPERATURES AND THE ATMOSPHERIC CIRCULATION IN THE NORTHERN HEMISPHERE

The advent of increasingly high-resolution satellite observations and numerical models has led to a series of advances in our understanding of the role of midlatitude sea surface temperature (SST) in climate variability, especially near western boundary currents (WBC). For example, recent observational analyses suggest that ocean dynamics play a central role in driving interannual SST variability over the Kuroshio-Oyashio and Gulf Stream Extension regions, and recent numerical experiments suggest that variations in the SST field in the Kuroshio-Oyashio Extension region may have a much more pronounced influence on the atmospheric circulation than previously thought.

We assess the observational support for (or against) a robust atmospheric response to midlatitude ocean variability in the Kuroshio-Oyashio and Gulf Stream Extension regions. We apply lead/lag analysis based on daily data to assess relationships between SST anomalies and the atmospheric circulation on transient timescales, building off of previous studies that have applied a similar methodology to weekly data. In addition, we employ a novel approach to separate the regressions into an “atmospheric forcing” pattern and an “atmospheric response” pattern through spatial linear decomposition.

The analysis reveals two distinct patterns associated with midlatitude atmosphere/ocean interaction in the vicinity of the major Northern Hemisphere WBCs: 1) a pattern that peaks 2-3 weeks before the SST anomalies (the “atmospheric forcing”) and 2) a pattern that peaks after the SST anomalies (the “atmospheric response”). The latter pattern is independent of the former, and is interpreted as the signature of SST variability in the atmospheric circulation. Further analysis is required to understand if the “atmospheric response” pattern truly reflects the response to the SST anomalies within the WBC regions.

ACKNOWLEDGEMENTS

The author would like to thank Dr. David W. J. Thompson of the Department of Atmospheric Science at Colorado State University for serving as an advisor and providing wisdom and guidance throughout the master's program. The author would also like to thank Dr. Elizabeth Barnes and Dr. Subhas Karan Venayagamoorthy for participating in the graduate committee and providing valuable insight. Finally, the author would like to thank her family and friends for their invaluable support.

This material is based on work supported by the National Aeronautics and Space Administration grant number NNX13AQ04G.

TABLE OF CONTENTS

Abstract	ii
Acknowledgements	iii
Table of Contents	iv
List of Figures	vi
1. Introduction and Background	1
1.1. Background: Midlatitude Ocean-Atmosphere Interactions	2
1.1.1. The Linear Response of the Atmosphere to Midlatitude SST	
Anomalies	2
1.1.2. The Thermodynamic Response of Midlatitude SST Anomalies	6
1.1.3. Review of Observational Studies	10
1.1.4. Review of Numerical Studies	14
1.2. Thesis Goal	19
2. Data and Methods	21
2.1. ECMWF ERA-Interim Data	21
2.2. SST Indices	21
2.3. Atmospheric Indices	23
2.4. Analysis Techniques	24
2.4.1. Linear Regression Analysis	24
2.4.2. Spatial Linear Decomposition	26
2.4.3. Significance Testing	27
3. Results	29
3.1. North Pacific	29
3.1.1. K_{SST} Index	29
3.1.2. PNA Index	39
3.2. North Atlantic	43

3.2.1. G_{SST} Index	43
3.2.2. NAM Index	55
3.2.3. G_{SLP} Index	59
4. Discussion and Conclusions	63
4.1. Discussion	63
4.1.1. North Pacific Circulation Results	66
4.1.2. North Atlantic Circulation Results	67
4.2. Conclusions	68
4.3. Future Work	71
4.3.1. Linearity of the Response	71
4.3.2. AMSR-E Observational Analysis	72
4.3.3. Numerical SST Experiments	73
References	74

LIST OF FIGURES

FIGURE 1.1	4
FIGURE 1.2	5
FIGURE 1.3	7
FIGURE 1.4	8
FIGURE 1.5	12
FIGURE 1.6	16
FIGURE 1.7	18
FIGURE 2.1	22
FIGURE 2.2	25
FIGURE 3.1	29
FIGURE 3.2	30
FIGURE 3.3	31
FIGURE 3.4	32
FIGURE 3.5	34
FIGURE 3.6	35
FIGURE 3.7	36
FIGURE 3.8	38
FIGURE 3.9	39
FIGURE 3.10	40
FIGURE 3.11	41
FIGURE 3.12	42
FIGURE 3.13	43
FIGURE 3.14	44
FIGURE 3.15	45
FIGURE 3.16	46
FIGURE 3.17	48
FIGURE 3.18	49
FIGURE 3.19	50
FIGURE 3.20	51
FIGURE 3.21	53
FIGURE 3.22	54
FIGURE 3.23	55
FIGURE 3.24	56
FIGURE 3.25	57
FIGURE 3.26	58
FIGURE 3.27	60
FIGURE 3.28	61
FIGURE 3.29	62
FIGURE 4.1	65

CHAPTER 1: INTRODUCTION AND BACKGROUND

The ocean is an integral part of the climate system. In the tropics, it is clear that variations in the ocean surface temperature directly affect the atmosphere. That is because at these latitudes, anomalies in sea surface temperatures (SST) are balanced by vertical motion since the horizontal gradients in temperature are small [*e.g.*, Hoskins and Karoly 1981]. As such, small changes in SSTs can lead to pronounced changes in the upper troposphere. In contrast, in the midlatitudes, the horizontal gradients in temperature are large, and thus small changes in SSTs are readily balanced by small changes in the horizontal wind fields. The midlatitude atmosphere is believed to drive variations in the SST field; whether it responds to variations in the SST field remains unclear [*e.g.*, Kushnir et. al. 2002 and authors therein].

SST variability can arise from atmospheric forcing or due to internal ocean forcing that is independent of the atmosphere, such as that found near western boundary currents (WBCs) [*e.g.*, Frankignoul and Reynolds 1983]. Western boundary currents are strong poleward flowing currents along the western side of an ocean basin that transport heat from the tropics to higher latitudes. The two main WBCs in the Northern Hemisphere are the Kuroshio Current in the North Pacific Ocean and the Gulf Stream Current in the North Atlantic Ocean. The Oyashio Current is also a WBC, except that it flows equatorward and advects subarctic SST to the midlatitudes where it joins the Kuroshio. The regions where these WBCs turn eastward are associated with tight north-south SST gradients with warmer water to the south and colder water to the north.

The goal of this thesis is to examine the relationships between midlatitude SST variability in the vicinity of WBCs and the midlatitude atmospheric circulation on daily timescales. In this chapter, Section 1.1 reviews relevant background information: subsections 1.1.1 and 1.1.2 introduce the basic dynamical and thermodynamical responses to midlatitude SST anomalies, respectively. The following subsections review observational (1.1.3)

and numerical (1.1.4) studies related to midlatitude air-sea interaction. The motivation and specific goals of the thesis are outlined in Section 1.2.

1.1. Background: Midlatitude Ocean-Atmosphere Interactions

1.1.1. The Linear Response of the Atmosphere to Midlatitude SST Anomalies

Hoskins and Karoly [1981] describe the steady-state dynamic response to an anomalous heat source in both the tropics and midlatitudes. As previously mentioned, SST anomalies in the tropics are balanced by vertical motion. This balance is explained by the linearized thermodynamic energy equation:

$$\bar{u} \frac{\partial \theta'}{\partial x} + v' \frac{\partial \bar{\theta}}{\partial y} + w' \frac{\partial \bar{\theta}}{\partial z} = \left(\frac{\theta_o}{g}\right) Q \quad (1)$$

where the first term on the left-hand side (LHS) is the advection of the anomalous east-west potential temperature gradient ($\frac{\partial \theta'}{\partial x}$) by the zonal-mean wind (\bar{u}), the second term on the LHS is the advection of the mean north-south temperature gradient ($\frac{\partial \bar{\theta}}{\partial y}$) by the anomalous meridional wind (v'), the third term on the LHS is the advection of the mean vertical potential temperature gradient ($\frac{\partial \bar{\theta}}{\partial z}$) by the anomalous vertical wind (w'), and the term on the right-hand side (RHS) represents heating (where Q is the diabatic heating). Primes denote perturbations and bars denote the basic state. In the tropics, advection due to the horizontal components of the wind (u and v) is smaller in comparison to that associated with the vertical component (w) due to the horizontally uniform temperature distribution there. Hence, the first two terms on the LHS of the linearized thermodynamic energy equation scale smaller compared to the third term in the tropics, and the vertical component of the temperature advection balances diabatic heating anomalies (*i.e.*, warm SST anomalies are balanced by rising motion).

The steady-state balance in the tropics does not hold for the extratropical atmosphere where the horizontal (especially meridional) temperature gradients are large. Here, anomalous diabatic heating is readily balanced by the meridional advection of the mean north-south temperature gradient. To understand the dynamic response to an anomalous heat source in the extratropics, Hoskins and Karoly [1981] also explored the linearized vorticity equation:

$$\bar{u} \frac{\partial \zeta'}{\partial x} + \beta v' = f \frac{\partial w'}{\partial z}. \quad (2)$$

where the first term on the LHS is the advection of the anomalous east-west gradient in vertical vorticity ($\frac{\partial \zeta'}{\partial x}$) by the zonal-mean wind (\bar{u}), the second term is the advection of the north-south gradient in planetary vorticity (β) by the anomalous meridional wind (v'), and the term on the RHS is the anomalous vertical stretching ($\frac{\partial w'}{\partial z}$) by the planetary vorticity (f). Again, primes denote perturbations and bars denote the basic state. Both the linearized thermodynamic energy and vorticity equations are required to understand the balance to a heating anomaly in the midlatitudes.

Figure 1.1 provides a simple schematic of the basic hydrostatic balance at midlatitudes. The anomalous heat source at the surface leads to the development of a “thermal low”. The anomalous surface heating warms the column of air directly above and forces the isentropes to rise locally. This local rise results in the formation of an upper-level high above the heat source. As air flows from high to low pressure, the ageostrophic component of the flow removes mass from the column, creating a low pressure at the surface.

Hoskins and Karoly [1981] find that thermodynamic balance requires the surface low to be shifted downstream (or to the east of the surface heating). The radiative imbalance between the tropics and the pole leads to warmer temperatures near the equator and cooler temperatures near the poles. Hence, the average north-south temperature gradient, $\frac{\partial \bar{\theta}}{\partial y}$, in the northern hemisphere is less than zero. This temperature gradient is generally large in comparison to the east-west and vertical temperature gradients, and thus $v' \frac{\partial \bar{\theta}}{\partial y}$ balances Q .

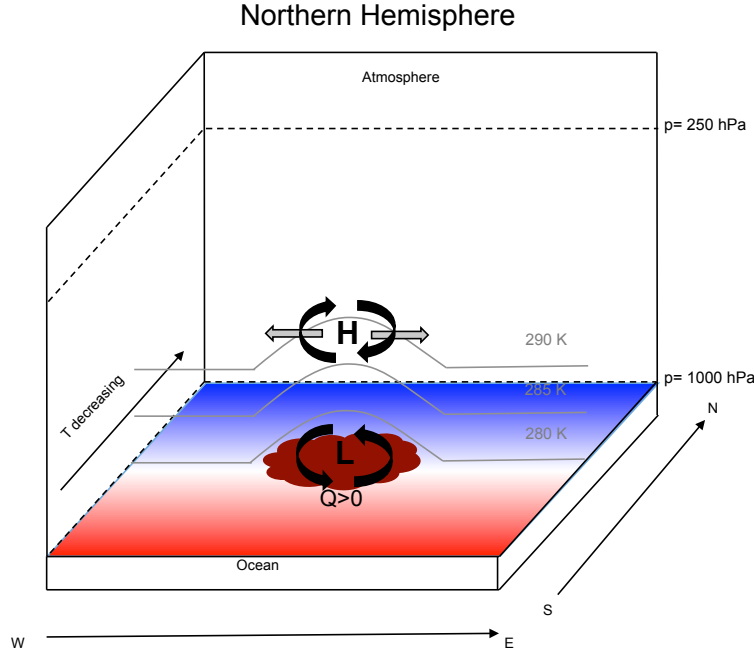
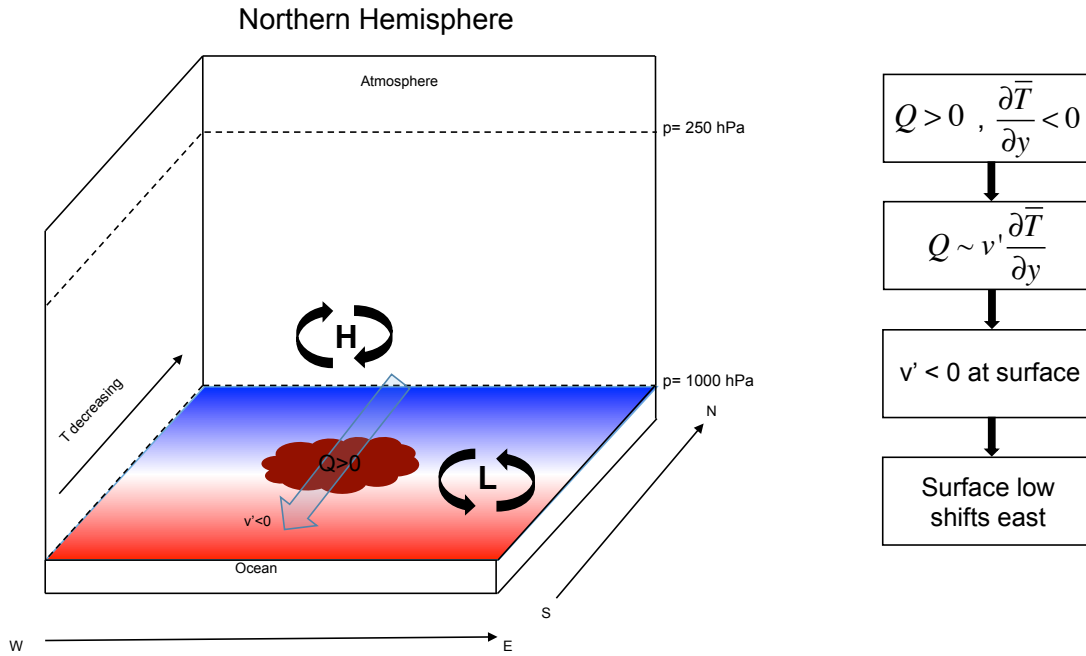


Figure 1.1. Basic hydrostatic balance for a heating anomaly in the extratropical Northern Hemisphere. Red (blue) shading indicates warm (cool) temperatures, and the dark red shading indicates the position of the heating anomaly. Thin gray contours represent the isentropes (in Kelvin) and thick gray arrows represent the ageostrophic flow. The thick black arrows represent the anomalous atmospheric circulation.

As $Q > 0$ and $\frac{\partial \bar{\theta}}{\partial y} < 0$, the anomalous meridional wind, v' , must be less than zero at the surface. With the wind blowing equatorward across the heat source, the surface low must shift to the east (Figure 1.2.a).

The linearized vorticity equation lends insight into the resulting changes in the surface circulation (Figure 1.2.b). At midlatitudes, the equation scales such that $\beta v' \sim f \frac{\partial w'}{\partial z}$, where $\beta, f > 0$ in the Northern Hemisphere. Since $v' < 0$ in a region of heating, the vertical stretching term, $\frac{\partial w'}{\partial z}$, must be less than zero above the heat source in order to balance the low-level creation of vorticity. Therefore, there must be sinking motion near the surface at the heating. As for the circulation aloft, recall that the vertical stretching term is less than zero near the surface. As w' decreases with height, the vertical motion goes to zero near the 500hPa level, and $\frac{\partial w'}{\partial z} > 0$ aloft. Since the meridional wind balances vertical stretching, $v' > 0$ aloft, resulting in poleward flow at upper levels above the surface heating. This results in an eastward shift of the upper level high.

(a) Thermodynamic Balance



(b) Vorticity Balance

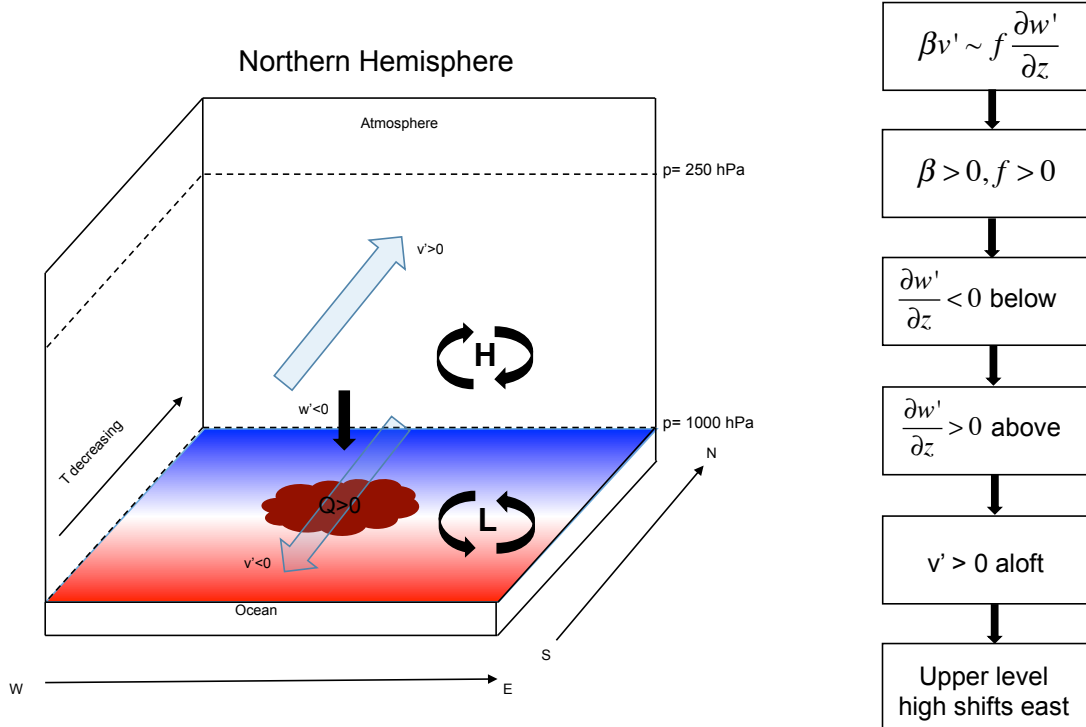


Figure 1.2. Atmospheric circulation response to a surface heating anomaly in the extratropical Northern Hemisphere based on a) thermodynamic balance and b) vorticity balance. The shading is the same as that described in Figure 1.1. Light blue arrows indicate the anomalous meridional flow, and the vertical arrows indicate the direction of vertical motion.

1.1.2. The Thermodynamic Response to Midlatitude SST Anomalies

Barsugli and Battisti [1998] revealed the basic thermodynamic response to midlatitude heating anomalies based on a simple stochastic coupled energy balance model. Their model branches off of the simple stochastic model of SST variability as described by Frankignoul and Hasselmann [1977]:

$$\frac{dT}{dt} = F - \lambda T, \quad (3)$$

where F represents mixed layer forcing anomalies, T is the sea surface temperature, and λ is a feedback parameter related to damping by surface fluxes. To create their thermally coupled model, Barsugli and Battisti [1998] consider the basic effects of coupling between the ocean and the atmosphere, as illustrated in Figure 1.3. The effects consist of net shortwave and longwave radiative heating of the atmosphere and ocean, combined surface turbulent latent and sensible heat fluxes, and dynamical forcing of the atmosphere (considered to be of stochastic nature). The energy balance is used to derive quantitative measures of coupling and damping in the system of equations. The key equations in the two-way coupled model (Eqns. 1-2 in Barsugli and Battisti [1998]) are analogous to the form:

$$\gamma_1 \frac{\partial T_a}{\partial t} = -\alpha_1 T_a - \beta_1 (T_a - T_o) + A \quad (4)$$

$$\gamma_2 \frac{\partial T_o}{\partial t} = -\alpha_2 T_o - \beta_2 (T_o - T_a) \quad (5)$$

where T_a is the atmospheric temperature, T_o is the ocean temperature, γ_1 is the heat capacity of the atmosphere, γ_2 is the heat capacity of the ocean, α_1 is a coefficient related to the radiative damping of the atmosphere, α_2 is a coefficient related to the radiative damping of the ocean, β_1 and β_2 are coefficients related to combined latent, sensible, and longwave heat fluxes (or coupling) between the atmosphere and ocean, and A represents atmospheric white noise. Eqn. 4 indicates that the rate of change of atmospheric temperature ($\frac{\partial T_a}{\partial t}$) is equal to the sum of atmospheric damping ($-\alpha_1 T_a$), ocean forcing ($-\beta_1 (T_a - T_o)$), and atmospheric

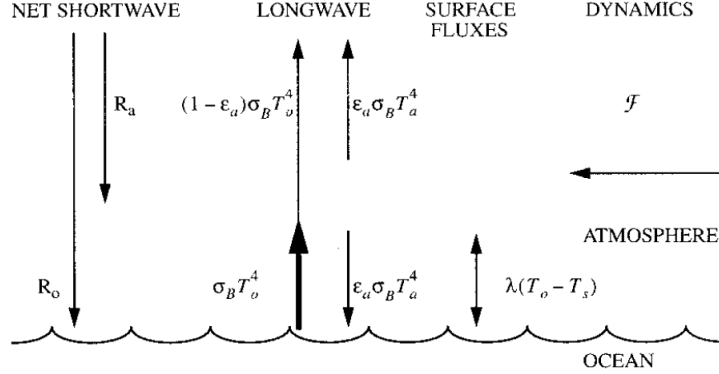


Figure 1.3. Courtesy of Barsugli and Battisti [1998]. Diagram of simple energy balance model. The atmosphere is treated as a single graybody layer with effective temperature, T_a , and longwave emissivity, ϵ_a , that is coupled to a slab ocean with temperature, T_o . R_o and R_a represent the incoming shortwave radiative heating of the ocean and atmosphere, respectively. λ is a proportionality constant between the combined surface turbulent latent and sensible heat fluxes and the air-sea temperature difference. \mathcal{F} represents the dynamical forcing of the atmosphere, assumed to be of stochastic nature.

white noise (A). Similarly, Eqn. 5 describes the rate of change of ocean temperature ($\frac{\partial T_o}{\partial t}$) that is equal to the sum of ocean damping ($-\alpha_2 T_o$) and atmospheric forcing ($-\beta_2(T_o - T_a)$). The coefficients α and β are not equal for the ocean and the atmosphere due to the difference in radiative balance between the two systems.

The coupled system is compared to an uncoupled system where there is one-way forcing from the atmosphere to the ocean. This one-way forcing serves as a basis for testing the effects of thermal coupling. In the coupled model, the coefficients in the system of equations as defined by Barsugli and Battisti [1998] are: $\gamma_1 = 1 \times 10^7 \frac{J}{m^2K}$, $\gamma_2 = 2 \times 10^8 \frac{J}{m^2K}$, $\alpha_1 = 2.8 \frac{W}{m^2K}$, $\alpha_2 = 1.9 \frac{W}{m^2K}$, $\beta_1 = 23.9 \frac{W}{m^2K}$, and $\beta_2 = 23.4 \frac{W}{m^2K}$. As for the uncoupled model, the coefficients remain the same, except $\beta_1 = 0$ since the atmospheric temperature is not affected by the ocean. The authors explain that dynamical forcing includes the effects of coupling and chose to resolve this problem by calculating a standard form of the above system of equations (Eqns. 6-7 in Barsugli and Battisti [1998]) with different coefficients. However, to keep the coefficients in physical units, we will treat the atmospheric forcing term, (A), as white noise forcing of unit amplitude and ignore the coupling component. This discrepancy should be kept in mind for interpreting the following results.

Autocorrelations

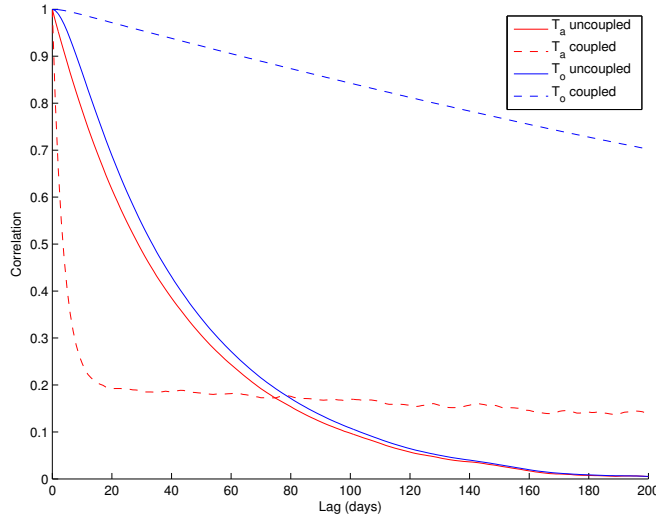


Figure 1.4. Autocorrelations of atmospheric (red) and oceanic (blue) temperature for an uncoupled (solid lines) and coupled (dashed lines) system of equations, as described by the models in Barsugli and Battisti [1998].

Autocorrelations of atmospheric and oceanic temperature between the two models are shown in Figure 1.4. The atmospheric and oceanic temperature are initialized at zero for each forcing scenario, and the equations are run out 500 years. It is clear from the results that in a coupled system, sea surface temperature persistence increases. While the atmospheric temperature in the coupled model initially decays more rapidly than the uncoupled model, it appears that the coupled temperatures become more persistent in the long-term. The autocorrelations are qualitatively similar but quantitatively different than those presented in Barsugli and Battisti [1998]. We attribute this discrepancy to our use of physically meaningful coefficients (which do not resolve the coupled component of atmospheric noise) compared to their standard form for solving the system of equations.

The coupled model experiment from the study indicated that coupling significantly increases the persistence of both atmospheric and oceanic temperature anomalies at low frequencies. The authors conclude that reduced internal damping of temperature anomalies due to surface heat fluxes is the physical mechanism responsible for the increased persistence. Compared to Hoskins and Karoly [1981] (who argue that anomalous midlatitude heating is

balanced by the meridional advection of the north-south temperature gradient), Barsugli and Battisti [1998] present a case for a direct thermodynamic response of the midlatitude ocean on the overlying atmosphere. However, the authors note the simplicity of the model experiment and caution that the results be taken as a conceptual understanding of midlatitude ocean-atmosphere coupling rather than a quantitative one.

The studies by Hoskins and Karoly [1981] and Barsugli and Battisti [1998] provide the basic framework for understanding how the atmosphere responds to a midlatitude heating anomaly at the surface in the long-term mean. Based on the linear response of the atmosphere, we expect a surface low and upper-level high to form downstream of a warm SST anomaly in the extratropics. As for the thermodynamic response, we expect that coupling due to combined latent and sensible heat fluxes will increase the persistence of both atmospheric and oceanic temperature anomalies. The background presented thus far provides a theoretical, mathematical basis for the expected atmospheric response to an imposed heat source in the midlatitudes.

Before we explore additional research related to midlatitude air-sea interaction, we want to point out a key study in contrast to those presented in the previous subsections. Brayshaw *et. al.* [2008] have suggested that it is the changes in the meridional SST gradient caused by a heating anomaly that is more important than the SST anomaly itself for understanding the atmosphere's response. In their study, the authors consider that a warm SST anomaly leads to increased baroclinicity on the poleward side (due to an enhancement in the SST gradient) and decreased baroclinicity on the equatorward side (due to a reduction in the SST gradient). A series of aquaplanet global climate model (GCM) simulations found that the subtropical jet and storm track are strengthened and shifted poleward of the warm SST anomaly. Hence, in addition to the basic dynamical and thermodynamical responses, an anomalous heating is also capable of influencing the baroclinicity in the midlatitude atmosphere through changes in the SST gradient.

1.1.3. Review of Observational Studies

As for earlier work in the air-sea interaction field, Kushnir *et. al.* [2002] compiled a review of more than 15 years of midlatitude ocean-atmosphere observational and numerical research prior to 2003. We will focus on the key findings from the observational studies by authors therein. Extratropical monthly and seasonal SST anomalies are well correlated with the dominant patterns of atmospheric variability, and the association is strongest when the atmosphere leads the ocean by approximately a month [*e.g.*, Davis 1976, 1978; Palmer and Sun 1985]. Typically, negative SST anomalies in the midlatitudes are associated with anomalously strong surface westerlies above (straddled by a cyclone poleward and an anticyclone equatorward of the surface westerlies) [*e.g.*, Wallace *et. al.* 1990]. Furthermore, wintertime circulation patterns associated with SST anomalies tend to display an equivalent barotropic vertical structure [*e.g.*, Frankignoul 1985].

As for the ocean leading the atmosphere, some studies found a statistically significant covariance between wintertime 500hPa heights and SST up to six months earlier [*e.g.*, Czaja and Frankignoul 2002; Rodwell and Folland 2002]. The atmospheric “response” displayed a NAM pattern, suggesting a link between SST reemergence and the leading mode of atmospheric variability in the Northern Hemisphere. The “reemergence mechanism” proposes that temperature anomalies form in the deep ocean mixed layer during the winter/spring season and then reemerge at the surface when the mixed layer deepens during the following fall/winter [*e.g.*, Alexander *et. al.* 1998]. Upon reviewing the observational (and modeling) studies prior to 2003, the authors of Kushnir *et. al.* [2002] concluded that while extratropical SST anomalies are found to influence the atmosphere, the responses are modest in comparison to internal atmospheric variability. Thus, the prevailing view on midlatitude air-sea interaction through 2002 was that the midlatitude ocean did not play a significant role in influencing the overlying atmospheric circulation.

Since 2002, the advent of increasingly high-resolution satellite observations has led to advancements in understanding the role of the midlatitude ocean in atmospheric variability. The QuikSCAT satellite radar scatterometer provides 25-km resolution measurements of near-surface wind speed and direction over the global ocean [*e.g.*, Chelton *et. al.* 2001]. Over the Southern Ocean, observations of wind stress curl and divergence indicated that surface air blowing across a SST front tended to accelerate the wind [*e.g.*, O’Neill *et. al.* 2003; Chelton *et. al.*, 2004, Chelton and Xie 2010]. The resulting divergence and convergence patterns support the hypothesis stated in Hayes *et. al.* [1989] that SST modification of the marine atmospheric boundary layer (MABL) induces perturbations in the surface winds through vertical turbulent mixing. The mechanism hypothesizes that an increase in SST reduces the static stability in the overlying column of air and intensifies vertical mixing, bringing faster winds from aloft to the surface [*e.g.*, Hayes *et. al.* 1989]. The vertical mixing mechanism was also supported by Nonaka and Xie [2003] who analyzed the covariability between SST and wind speed over the Kuroshio Extension east of Japan. They identified four major positive SST anomaly centers along the Kuroshio that are collocated with a local enhancement of wind speed. Steady ocean currents were further discovered to influence persistent small-scale features in the curl and divergence of wind stress which could not previously be resolved in ocean measurements [*e.g.*, Chelton *et. al.* 2004]. The studies mentioned above provide observational evidence for a direct response in surface winds to anomalous SST in the midlatitudes (especially near ocean fronts) that has only recently been noticed due to the availability of higher resolution satellite measurements.

In addition to the vertical mixing mechanism, evidence has been found in support of the pressure adjustment mechanism for understanding midlatitude ocean influence. Observational studies on the Gulf Stream suggested a consideration of this mechanism for explaining the convergence and divergence of the surface wind field near ocean fronts [*e.g.*, Minobe *et. al.* 2008, 2010]. The pressure adjustment mechanism hypothesizes that SST modifies MABL air temperature. Relatively high pressure forms over the colder flank of the ocean front while

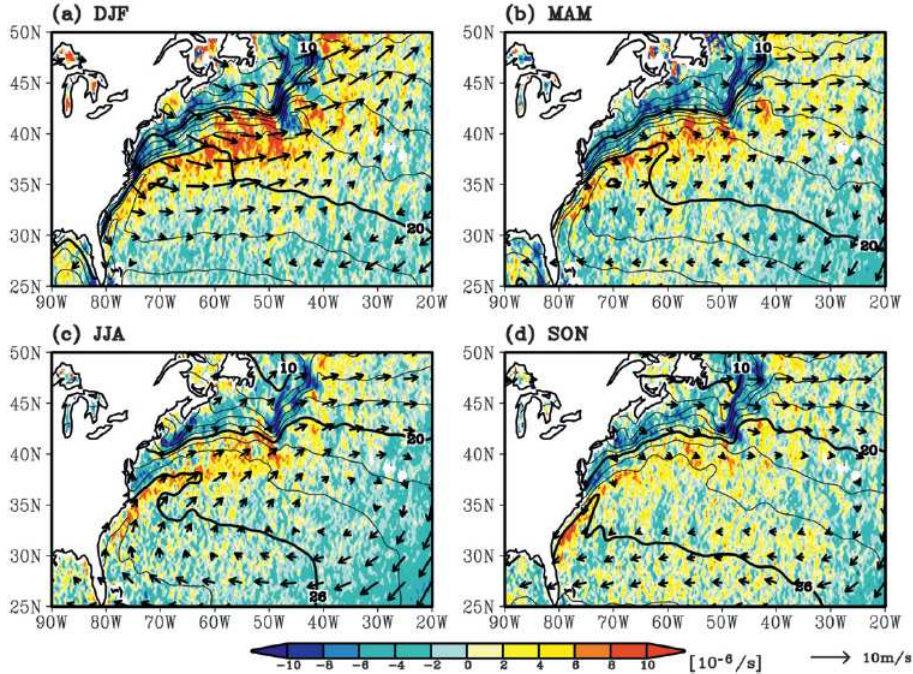


Figure 1.5. Courtesy of Minobe *et. al.* [2010]. Observed seasonal mean SST (contours) and QuikSCAT near-surface wind velocities (vectors) and convergences (color).

relatively low pressure forms over the warmer flank. This pressure difference induces cross-frontal flow in the surface wind, leading to divergence on the colder side of the front and convergence on the warmer side, as seen in QuikSCAT observations in Figure 1.5. Surface convergence then forces vertical motion. Both studies found evidence from satellite observations of a narrow rain band that appeared anchored to the surface wind convergence. Minobe *et. al.* [2010] argue that the diabatic heating over the Gulf Stream leads to ascent, which contrasts the prevailing view of Hoskins and Karoly [1981] that diabatic heating is balanced by the horizontal advection of temperature gradients in the extratropics. Furthermore, Minobe *et. al.* [2008, 2010] expanded on results presented in the previous studies (O'Neill *et. al.* 2003; Nonaka and Xie 2003; Chelton *et. al.* 2004; etc) by showing that the effect of anomalous SST on surface winds extends into the free troposphere.

Aside from the vertical mixing and pressure adjustment mechanisms, shifts in the locations of the ocean fronts are also argued to influence the atmosphere. Nakamura *et. al.* [1997] noted a region of strong SST variability in the North Pacific that is associated

with the subarctic front, where the cold Oyashio Current adjoins the warm Kuroshio Extension near 42°N . The authors found that SST anomalies in this region tended to occur simultaneously with the Pacific North American (PNA) pattern, which is the second leading mode of atmospheric variability in the Northern Hemisphere [*e.g.*, Wallace and Gutzler 1981; Quadrelli and Wallace 2004]. Meridional shifts in both the Kuroshio Extension (KE) and Oyashio Extension (OE) fronts were found to have significant impacts on the large-scale atmospheric circulation [*e.g.*, Frankignoul *et. al.* 2011]. A northward shift in the OE front was found to precede an equivalent barotropic signal reminiscent of the positive phase of the North Pacific Oscillation (NPO) pattern (and the negative phase for a southward shift). As for the KE front, an equivalent barotropic high in the northwestern North Pacific responds to a northward shift, with a weaker low in the Kuroshio-Oyashio Extension (KOE) region. In addition to the Kuroshio and Oyashio Extensions in the North Pacific, Kwon and Joyce [2013] investigated the impacts of meridional shifts in the Gulf Stream on the atmosphere. Their observational analysis indicated that northward shifts in all three fronts are followed by a weakening of the synoptic storm tracks. Furthermore, the authors found that one to three years prior to the shifts in the ocean fronts, the atmospheric storm tracks shift north and intensify. These observational studies suggest the importance of ocean fronts for not only influencing the near-surface winds, but also the large-scale circulation.

Motivated by the supporting evidence presented for midlatitude SST influence over the past decade, this thesis builds on two primary past observational studies of midlatitude atmosphere-ocean interaction on transient timescales. Deser and Timlin [1997] investigated wintertime air-sea interaction in the North Atlantic and Pacific sectors using lead/lag relationships on weekly timescales. Lead/lag analysis is beneficial for understanding how the relationships between two variables (*i.e.*, the ocean and the atmosphere) evolve. The authors found a sharp asymmetry in covariability between the extratropical atmosphere and the SST field, with minimum covariability when SST leads by 2 weeks and maximum covariability when the atmosphere leads by 2-3 weeks. The results indicated that SST anomalies forced

by the midlatitude atmospheric circulation should be expected to peak several weeks after the maximum atmospheric forcing (at which point SST damping will outweigh atmospheric forcing). Ciasto and Thompson [2004] conducted a similar study where lead/lag relationships were investigated between North Atlantic SST anomalies and the Northern Annular Mode (NAM). The seasonal mean and each winter’s mean were removed from the weekly data to isolate processes that occur on subseasonal timescales. The NAM was found to lead the North Atlantic SST “tripole” pattern by approximately 2 weeks, consistent with results by Deser and Timlin [1997]. However, their results also indicated a statistically significant pattern of SST variability over the Gulf Stream region that preceded the NAM on intraseasonal timescales. Based on the analysis, the authors were unable to determine if the NAM responds to variations in SST over this region. We will extend the analyses of these two studies by investigating lead/lag relationships on daily timescales. As detailed in the above studies, lead/lag analysis provides evidence for assessing the relationship between two variables with respect to forcing and response.

1.1.4. Review of Numerical Studies

In addition to observational research, a variety of numerical studies have investigated relationships between the ocean and the atmosphere in the midlatitudes. As mentioned in the previous section, Kushnir *et. al.* [2002] also provided a review of global climate model (GCM) experiments performed over the decade and a half prior to 2002. These GCM studies can be categorized into three groups: 1) “idealized” experiments with fixed SST anomalies, 2) experiments with realistic, time-varying SST anomalies, and 3) coupled models where the ocean and atmosphere interact.

In the first category, atmospheric response patterns to fixed SSTs yielded varying results between baroclinic [*e.g.*, Kushnir and Held 1996] and equivalent barotropic patterns [*e.g.*, Palmer and Sun 1985; Peng *et. al.* 1995]. A key study by Palmer and Sun [1985] found

an approximate linear response of the atmosphere to prescribed midlatitude SST anomalies in the north-west Atlantic, though the response was weaker in comparison to tropical SST anomalies. The approach in the second category provides an opportunity to compare GCMs forced with historically observed SST variations directly with the true atmospheric circulation. The main contribution of these experiments was to better quantify the relative importance of internal and SST-forced variability [*e.g.*, Kushnir *et. al.* 2002]. While there was evidence of SST forced variance in the midlatitudes, a major caveat to this result was the discovery that extratropical SST anomalies included influence by tropical SST anomalies, diluting the understanding of an atmospheric response to the midlatitude ocean [*e.g.*, Lau and Nath 1994; Graham *et. al.* 1994]. On the other hand, when applying the same method to an ocean model by using historic atmospheric observations, the hindcasting experiments successfully predicted the evolution of SST anomalies, suggesting that the prime direction of forcing is from the atmosphere to the ocean [*e.g.*, Haney 1985; Battisti *et. al.* 1995]. As for the coupled models, the general consensus found that coupling increases the low-frequency atmospheric variance and persistence of atmospheric anomalies, consistent with the results from Barsugli and Battisti [1998]. Results from the numerical studies reviewed in Kushnir *et. al.* [2002] (again with the observational studies) provided little evidence supporting robust midlatitude SST forcing of the atmosphere outside of internal variability.

Numerical studies over the recent decade have since found new evidence for midlatitude ocean-atmosphere interaction. An experiment by Brayshaw *et. al.* [2008] suggested that a midlatitude heating anomaly is more important for changing the meridional SST gradient, which may be key for understanding the midlatitude atmospheric response. Results from their study indicated that increases in the midlatitude SST gradient (and thus the surface baroclinicity) generally lead to stronger storm tracks that shift slightly poleward. Minobe *et. al.* [2008, 2010] also used an atmospheric global climate model (AGCM) to conduct an experiment comparing the sharp SST front in the Gulf Stream to smoothed SST contours. The model was successful in recreating the narrow rainband in the vicinity of the

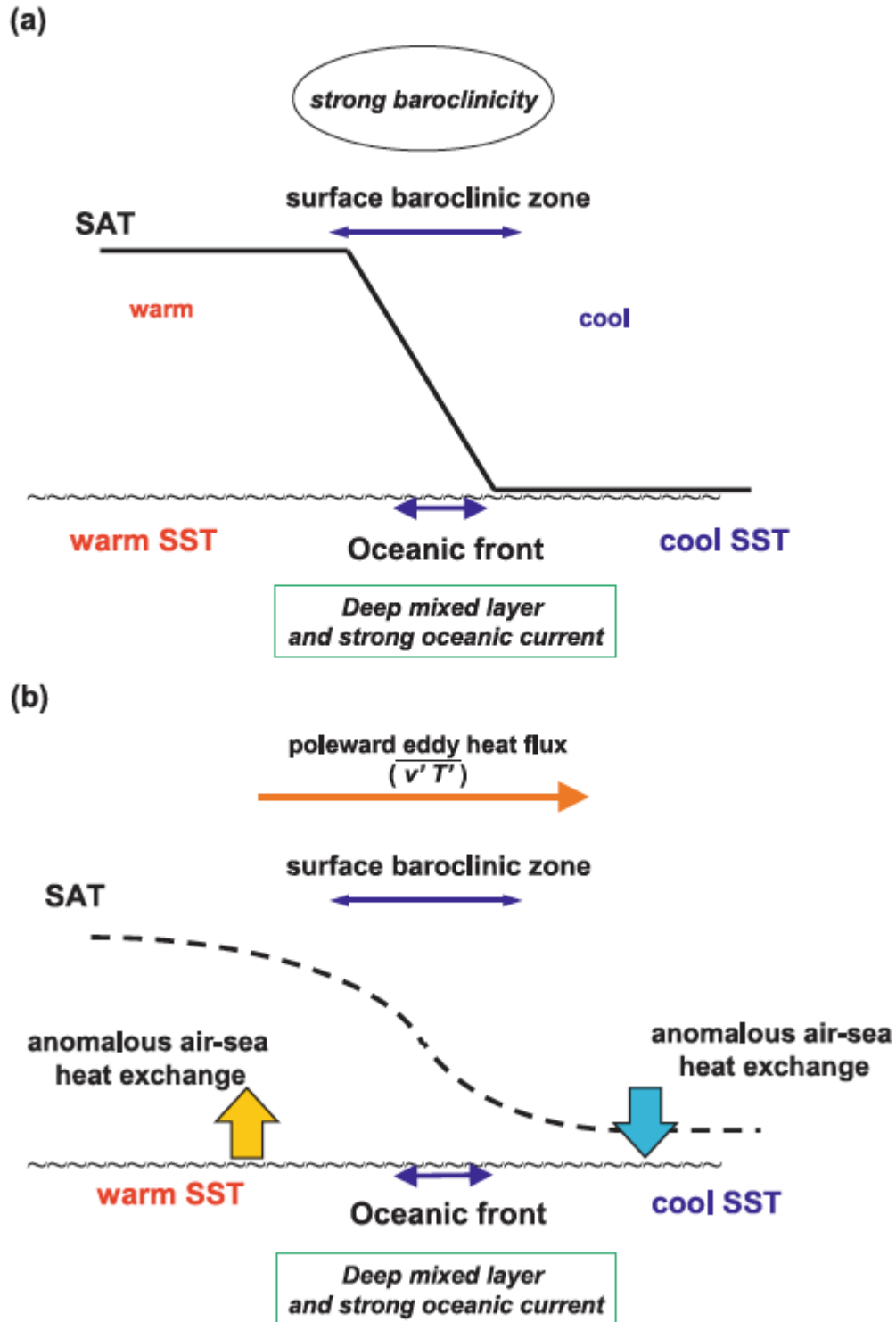


Figure 1.6. Courtesy of Sampe *et. al.* [2010]. Schematic showing the formation and restoration of surface baroclinicity by a) the strong SAT gradient resulting from the underlying ocean and b) poleward eddy heat fluxes that relax the SAT gradient which is restored by heat flux from the ocean.

Gulf Stream when forced with the observed SSTs. When the model was forced with the smoothed SST contours, the rainband disappeared, suggesting that the presence of tight SST gradients forces the precipitation, consistent with observations by Minobe *et. al.* [2008]. Nakamura *et. al.* [2008] conducted midlatitude front/no front experiments with respect to the storm tracks using an AGCM. The no front experiment showed reduced storm track activity that caused a weakening of midlatitude westerlies. The study highlighted the potentially important role of an ocean front in anchoring storm track activity by restoring sharp cross-frontal surface air temperature (SAT) gradients, thus restoring the baroclinicity. Similar results were found by Sampe *et. al.* [2010] who proposed a physical mechanism that explains the importance of the ocean front on the near-surface baroclinicity, as seen in Figure 1.6. The underlying SST influences the overlying atmosphere, creating a tight SAT gradient that leads to the development of baroclinic eddies. The SAT gradient is relaxed by poleward eddy heat fluxes that serve to reduce the near-surface baroclinicity. As the SAT gradient is reduced, anomalous air-sea heat exchange acts to restore the baroclinicity, effectively anchoring the storm track. These ocean front studies highlight the importance of the strength and location of regions of tight SST gradients for influencing the surface baroclinicity and storm tracks in the midlatitude atmosphere.

Alternative to the front/no front experiments, Smirnov *et. al.* [2014a,b] investigated both air-sea coupling and atmospheric responses to shifts in an ocean front using simple models and coupled GCMs. The first study utilized a local, coupled model similar to that of Barsugli and Battisti [1998] to analyze ocean-atmosphere coupling, except that both oceanic and atmospheric temperatures were subject to stochastic forcing [*e.g.*, Smirnov *et. al.* 2014a]. The analysis was extended to two simulations of the Community Climate System Model, version 3.5 (CCSM3.5), where the ocean models differed between high (0.1°) and low (1°) resolutions. Results from the study found that local coupling varied strongly over the North Pacific basin, becoming more important towards the eastern part of the basin. In the uncoupled model, atmospheric temperature variability remained relatively unchanged while

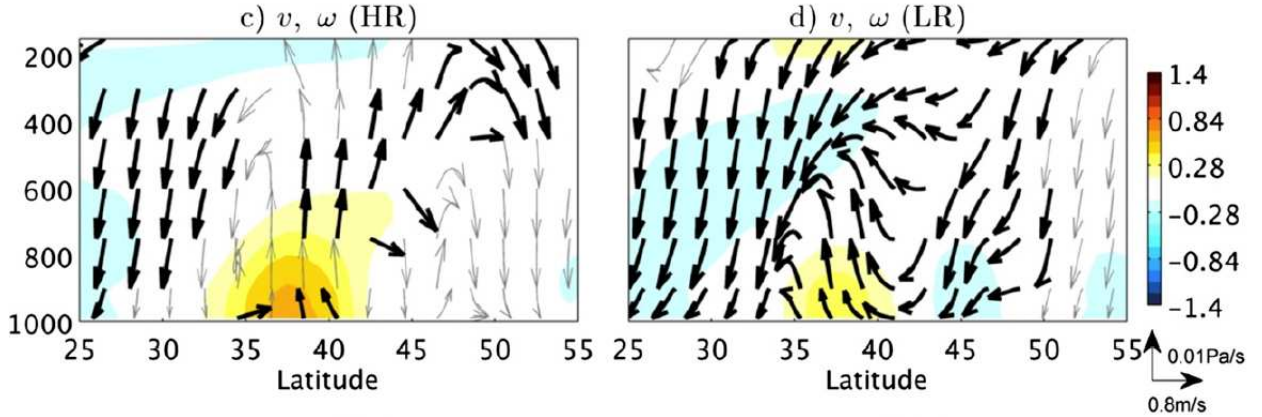


Figure 1.7. Courtesy of Smirnov *et. al.* [2014b]. Comparison of the wintertime atmospheric response to a midlatitude frontal shift between c) high-resolution (HR) and d) low-resolution (LR) model runs over the zonally averaged ($145^\circ - 165^\circ\text{E}$) SST front. Shading represents potential temperature and vectors represent the meridional and vertical wind circulation.

SST varied only near the WBC region. In this region, the authors approximated that 50% of monthly SST variability appears intrinsic to the ocean.

Furthermore, the study found that model resolution impacted the results. The high-resolution model better reproduced the latitude of maximum variability within the WBC while the low-resolution model had a more realistic representation of SST variability. Though one model was not clearly superior to the other, the results indicated the importance of model resolution for properly resolving ocean eddies. The importance of high-resolution GCMs was also noted when investigating the atmospheric response to shifts in the Oyashio Extension SST front [*e.g.*, Smirnov *et. al.* 2014b]. An AGCM was forced with prescribed SST anomalies corresponding to a north (or south) shift in the North Pacific for both high (0.25°) and low (1°) resolution versions of the CAM5. The atmospheric response to the meridional shifts for each model resolution is shown in Figure 1.7. The low-resolution model showed a strong horizontal atmospheric response with surface heating balanced by the mean equatorward flow, consistent with the paradigm for midlatitude heating described by Hoskins and Karoly [1981]. As for the high-resolution model, meridional shifts of the SST front showed an atmospheric response with stronger and deeper vertical motion as well as transient eddy moist static energy flux (not shown). Based on the differing results between the models,

the authors concluded that higher resolution GCMs will likely be key for improving our understanding of the effects of SST anomalies on the midlatitude atmospheric circulation. The experiments conducted in Smirnov *et. al.* [2014a,b] provide compelling evidence for SST forcing on the midlatitude atmospheric circulation in the North Pacific that serve as a motivation for the thesis.

A final key paper over the recent decade by Deser *et. al.* [2004] provided inspiration for one of the observational techniques used in our project. In their research, version 3 of the Community Climate Model (CCM3) was used to analyze the wintertime geopotential height response to observed patterns of monthly SST and sea ice trends. The responses were decomposed into two parts: an “indirect response” that represents the portion that projects onto the leading mode of variability and the “direct response” that represents the residual portion. Results from the study showed that the indirect response dominated the total simulated geopotential height pattern in the North Atlantic, resembling the leading mode of Northern Hemisphere atmospheric variability (the NAM). Though weaker, the direct response indicated a baroclinic structure in the vertical, with a surface low over the warm SST anomaly and a barotropic high slightly downstream. While the baroclinic structure was of opposite sign between positive and negative SST anomalies, the magnitudes were nonlinear. The authors hypothesize that this discrepancy is likely due to the stabilizing effect of surface cooling versus the destabilizing effect of surface warming. In our observational analysis, we will apply a similar “decomposition” to that described in Deser *et. al.* [2004] in an attempt to identify relationships to regions of SST variability that are intrinsic to the ocean, as suggested by Smirnov *et. al.* [2014a].

1.2. Thesis Goal

As summarized in this chapter, observational and numerical studies in the field of mid-latitude air-sea interaction through recent years have found that 1) the atmosphere forces

the ocean dominantly, 2) coupling between the ocean and the atmosphere increases the persistence of atmospheric anomalies, and 3) ocean fronts (regions of tight SST gradients) are capable of influencing the MABL. We have reviewed studies over the past decade that considered the key effects of midlatitude SSTs associated with ocean fronts on the wintertime “climatology” of the atmosphere [*e.g.*, Chelton *et. al.* 2004; Brayshaw *et. al.* 2008; Nakamura *et. al.* 2008; Minobe *et. al.* 2008, 2010; Sampe *et. al.* 2010]. Results from these studies suggest that ocean fronts are capable of influencing the MABL at the surface and into the free troposphere as well as affecting the surface baroclinicity and storm tracks. More recent work by Smirnov *et. al.* [2014a,b] has provided tantalizing evidence that suggests the importance of SST anomalies in the vicinity of western boundary currents (where tight SST gradients are present) for influencing the overlying atmospheric circulation. Results from their high-resolution experiments revealed a vertical response to warm SST anomalies in the midlatitudes, testing the prevailing view presented in Hoskins and Karoly [1981].

The aim of this thesis is to re-examine observational evidence for midlatitude ocean-atmosphere interaction in the daily-mean data in light of the research presented in this chapter. This work ties back to and builds off of previous studies by Deser and Timlin [1997] and Ciasto and Thompson [2004] who explore lead/lag relationships between the ocean and the atmosphere on weekly timescales. With respect to the recent supporting evidence for midlatitude SST forcing, we will revisit the lead/lag analysis using daily data since, presumably, the atmospheric response (if any) will set up on approximately weekly timescales. We will assess the observational support for (or against) a robust atmospheric response to midlatitude variability in the two major Northern Hemisphere western boundary currents: the Kuroshio-Oyashio (North Pacific) and the Gulf Stream (North Atlantic). The results will provide an observational basis for interpreting climate simulations of the atmospheric response to variations in SST. Chapter 2 explains the data and methods used in the thesis, and Chapter 3 highlights the results of the observational analysis. Finally, Chapter 4 discusses and summarizes the key findings and provides an outline for areas of future research.

CHAPTER 2: DATA AND METHODS

2.1. ECMWF ERA-Interim data

In order to perform the observational analyses, ECMWF ERA-interim data was obtained from the ECMWF data server for the January 1, 1979 - December 31, 2013 period. The variables analyzed in this project include 4xdaily sea surface temperature (SST), 850hPa meridional wind (v_{850}), 850hPa temperature (T_{850}), sea level pressure (SLP), and geopotential height at the 500hPa level (Z_{500}). Each variable is available at a spatial resolution of $1.5^\circ \times 1.5^\circ$ across the globe.

The signatures of baroclinic wave activity were estimated as follows: 1) the zonal mean was subtracted from both 6-hourly v_{850} and T_{850} in order to form the eddy components of those fields (denoted v_{850}^* and T_{850}^* , where asterisks represent deviations from the zonal mean); 2) a 10-day high-pass filter was applied to the eddy fields to isolate transient variability on synoptic timescales, and 3) the product of high-pass filtered v_{850}^* and T_{850}^* was taken to create the high-pass filtered transient eddy heat flux ($v^*T_{850}^*$).

The 4xdaily SST, $v^*T_{850}^*$, SLP, and Z_{500} fields were averaged to form daily and monthly-mean forms of the data. Anomalies were formed by removing the long-term mean seasonal cycles from the data. SLP anomalies were multiplied by a conversion factor of $8\frac{\text{m}}{\text{hPa}}$ (based on the hypsometric equation) to convert them to geopotential height at the 1000hPa level (Z_{1000}); this allows the surface and 500hPa level height anomalies to be compared in the same units. The results in this analysis will be presented in anomaly form.

2.2. SST indices

Throughout the study, we will rely on two primary SST indices, both of which explain variations in SSTs over the two major Northern Hemisphere western boundary current regions during the winter season months of November to March. The WBCs of interest

include the Kuroshio-Oyashio Extension and Gulf Stream Extension located in the North Pacific ($111^{\circ}\text{E} - 111^{\circ}\text{W}$, $24^{\circ}\text{N} - 78^{\circ}\text{N}$) and North Atlantic ($90^{\circ}\text{W} - 0^{\circ}$, $24^{\circ}\text{N} - 60^{\circ}\text{N}$) ocean basins, respectively. The indices are found by identifying regions of maximum SST variability within these basins.

Figures 2.1.a-b show the standard deviation in SST (σ_{SST}) over the North Pacific and North Atlantic sectors. For reference, the DJF climatological-mean SST for each region is depicted in Figures 2.1.c-d. It is evident that the regions of maximum variability coincide with the locations of the WBCs present in each basin, as indicated by the collocation of the regions of maximum σ_{SST} and large SST gradients. The region of SST variability located in the eastern North Pacific is associated with ENSO and is not part of the Kuroshio current system [*e.g.*, Nakamura *et. al.* 1997; Diaz *et. al.* 2001 and authors therein]. Based on the top two panels in Figure 2.1, we have defined the SST indices as averages over the boxed regions ($140^{\circ}\text{E} - 180^{\circ}\text{W}$, $34.5^{\circ}\text{N} - 42^{\circ}\text{N}$) for the Kuroshio-Oyashio Extension in the North Pacific

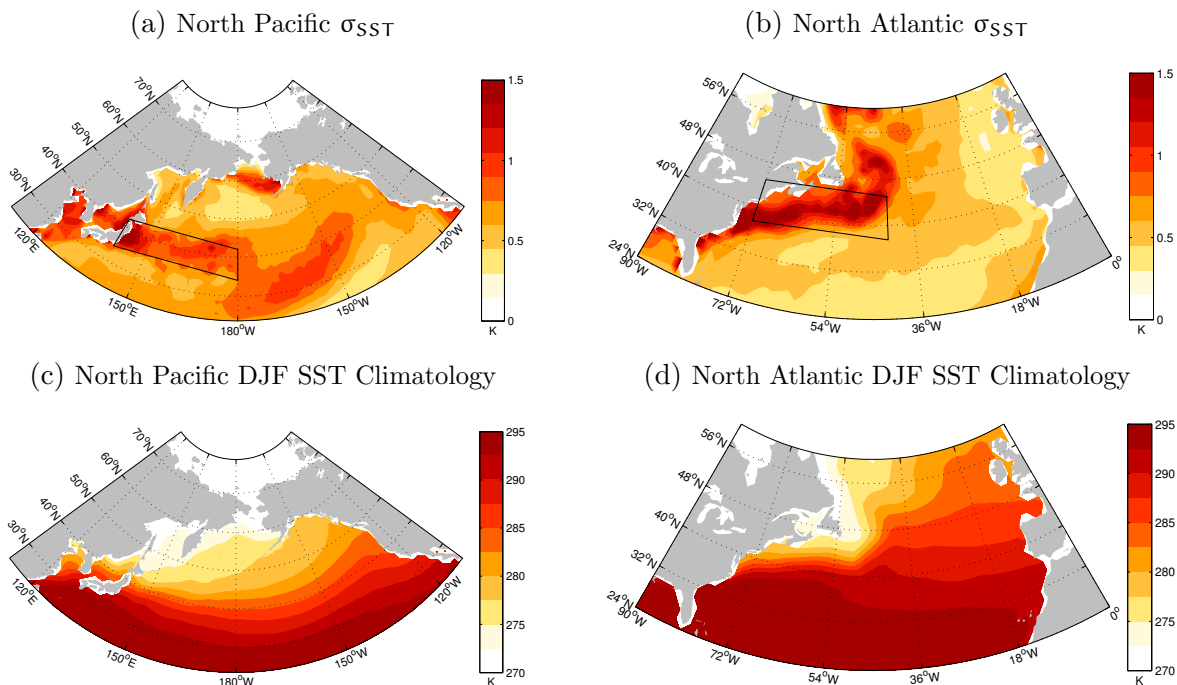


Figure 2.1. Winter (DJF) season SST standard deviation (a-b) and SST climatologies (c-d) for the North Pacific and North Atlantic, respectively. The boxes in a-b) indicate the regions averaged to calculate the K_{SST} and G_{SST} indices, respectively.

and $(72^\circ\text{W} - 42^\circ\text{W}, 37.5^\circ\text{N} - 45^\circ\text{N})$ for the Gulf Stream Extension in the North Atlantic. The averages are cosine-weighted to account for the decrease in area towards the poles. Each SST time series was averaged spatially over their respective box for the winter season (both monthly and daily) and standardized to create the Kuroshio-Oyashio (K_{SST}) and Gulf Stream (G_{SST}) SST indices. By definition, each standardized time series has a mean of zero and standard deviation of one. The SST indices are multiplied by a factor of -1 so that positive values denote below-normal SST, and vice versa.

2.3. Atmospheric indices

In contrast to the SST indices, this project also considers key atmospheric indices for each region: the Pacific/North American (PNA) pattern for the North Pacific and the Northern Annular Mode (NAM) for the North Atlantic. These are the two leading modes of atmospheric variability in the Northern Hemisphere for the DJF period based on the leading empirical orthogonal functions (EOFs) of monthly-mean SLP, where EOF1 corresponds to the NAM and EOF2 corresponds to the PNA [*e.g.*, Wallace and Gutzler 1980; Quadrelli and Wallace 2004].

To create the time series for each atmospheric index, EOF analysis was performed on the monthly SLP anomalies over the Northern Hemisphere. The time-mean was subtracted from the data and cosine-weighting was applied to account for the decrease in area towards the poles. As the leading two modes of atmospheric variability occur in the winter season [*e.g.*, Wallace and Gutzler 1980; Quadrelli and Wallace 2004], the analysis is performed over the DJF period. The data was organized into a matrix $\underline{\mathbb{X}}$ with dimensions M in time by N in space in order to calculate the spatial covariance matrix,

$$\underline{\mathbb{C}} = \frac{1}{N} \underline{\mathbb{X}} \underline{\mathbb{X}}^T. \quad (6)$$

The principal component (PC) time series are obtained by eigenanalyzing the spatial covariance matrix, $\underline{\mathbb{C}}$:

$$\underline{\mathbb{C}}\underline{\mathbb{E}} = \underline{\mathbb{E}}\underline{\mathbb{\Lambda}}. \quad (7)$$

Here, the PCs of the covariance matrix are contained in the columns of matrix $\underline{\mathbb{E}}$ and the corresponding eigenvalues are contained in the diagonal of matrix $\underline{\mathbb{\Lambda}}$. The PC time series explain the temporal evolution of the EOF patterns. However, as monthly SLP anomalies were used to perform the EOF analysis, the PCs only explain the monthly evolution of the patterns. To obtain the daily PC time series, the first two eigenvectors (EOF1 and EOF2) were calculated by regressing matrix $\underline{\mathbb{X}}$ onto PC1 and PC2, respectively. The EOFs were then projected onto the cosine-weighted daily field of SLP to obtain the daily-resolution indices. The resulting time series were standardized, with PC1 representing the NAM and PC2 representing the PNA.

2.4. Analysis Techniques

2.4.1. Linear Regression Analysis

To analyze potential relationships between the atmosphere and the Kuroshio-Oyashio Extension, regression maps were created for each variable in the North Pacific by calculating a linear fit of the form

$$\hat{\mathbf{y}} = \mathbf{a}_1\mathbf{x} + \mathbf{a}_0. \quad (8)$$

The variable $\hat{\mathbf{y}}$ represents an estimate of the variable (*i.e.*, SST) based on a linear relationship with \mathbf{x} (*i.e.*, the SST index). The regression coefficient, \mathbf{a}_1 , is the slope of the straight line and \mathbf{a}_0 is the y-intercept; the values of \mathbf{a}_1 and \mathbf{a}_0 are chosen to reduce the error between \mathbf{y} and $\hat{\mathbf{y}}$ (*i.e.*, the true SST and estimated SST, respectively). Using the method of least squares, the formulas for \mathbf{a}_1 and \mathbf{a}_0 are defined as:

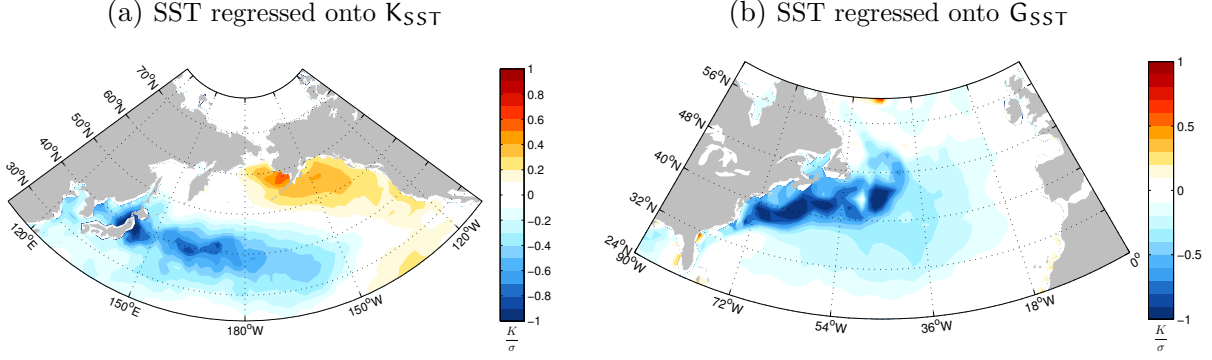


Figure 2.2. Monthly-mean SST regressed onto a) K_{SST} in the North Pacific and b) G_{SST} in the North Atlantic. Units are in Kelvin per standard deviation.

$$\mathbf{a}_1 = \frac{\overline{\mathbf{x}'\mathbf{y}'}}{\overline{\mathbf{x}'^2}} \quad (9)$$

$$\mathbf{a}_0 = \bar{\mathbf{y}} - \mathbf{a}_1\bar{\mathbf{x}}. \quad (10)$$

From Eqn. 9, we see that the regression coefficient, \mathbf{a}_1 , is equal to the covariance between \mathbf{x} and \mathbf{y} divided by the variance of \mathbf{x} . The regression maps are plotted using the calculated values of \mathbf{a}_1 at each grid point. As \mathbf{x} , or the index, is standardized, the units of \mathbf{a}_1 will be in $\frac{\text{unit}}{\sigma}$ (depending on the variable).

Initially, monthly SST, $\mathbf{v}^*\mathbf{T}_{850}^*$, \mathbf{Z}_{1000} , and \mathbf{Z}_{500} anomalies were regressed on the SST index at each grid point within the region. Figures 2.2.a-b show examples of the anomalous monthly SST regressed against K_{SST} and G_{SST} . It is clear that the cold SST anomalies in each basin are strongest over the regions where the SST indices were defined. This result is expected as SST in these regions should vary closely with the defined SST indices. In addition, there is an indication of warm SST anomalies in the North Pacific; thus, the regression onto K_{SST} illustrates a potential relationship between cold SST around the Kuroshio-Oyashio and warm SST to the south of Alaska. These regression maps will help identify if there is a connection between the variables and ocean/atmosphere indices.

In addition to contemporaneous regression, we also perform lead/lag regressions to evaluate the time lags between variations in the atmosphere and the SST field. The daily

anomalies for each variable were used to calculate regressions spanning lags from -20-days to +20-days (at 10-day intervals) during the winter time period, with negative lags including the month of November and positive lags including the month of March (K_{SST} remains constant at DJF). Thus, signals at negative lags are indicative of the basis time series (the predictor in the regression) leading the index, and signals at positive lags are indicative of the basis time series lagging the index. For example, when considering an ocean index, $\mathbf{v}^*T_{850}^*$, Z_{1000} , and Z_{500} negative lag patterns can be interpreted as the atmosphere preceding the ocean and vice versa for positive lags.

2.4.2. Spatial Linear Decomposition

We also decompose regression maps into components linearly congruent with patterns assumed to reflect the atmosphere forcing the ocean. To do so, the maps at all lags (hereafter referred to as \mathbf{map}_{lag}) were decomposed into two parts: a component linearly congruent with \mathbf{map}_{-20} (assumed to reflect the “atmospheric forcing”) and a residual component (assumed to reflect the “atmospheric response”). This technique is analogous to a linear fit of the form

$$M(\phi, \theta, t) = \alpha(t) \cdot M_{-20} + M_r(\phi, \theta, t), \quad (11)$$

where ϕ is longitude, θ is latitude, and t is time. M represents the full \mathbf{map}_{lag} regression and is a function of space and time (where time is the lag). The αM_{-20} term is the component of \mathbf{map}_{lag} that is linearly congruent with \mathbf{map}_{-20} , so M_{-20} represents \mathbf{map}_{-20} while α is a coefficient that is a function of lag (or time). The final term, M_r , is the residual part of the \mathbf{map}_{lag} regression and is a function of both space and time. The coefficient, α , is a “spatial” regression coefficient based on a least squares best fit and is defined as

$$\alpha_{lag} = \frac{\overline{\mathbf{map}_{lag} \cdot \mathbf{map}_{-20} \cdot W}}{\overline{\mathbf{map}_{-20} \cdot \mathbf{map}_{-20} \cdot W}}, \quad (12)$$

where W is the cosine-weighted latitude-longitude matrix. By this definition of α , the residual of \mathbf{map}_{-20} to \mathbf{map}_{-20} is zero.

In our analysis, the spatial linear decomposition can be thought of as follows. The component that is linearly congruent with \mathbf{map}_{-20} (αM_{-20}) is considered a “fit” to the atmospheric signal that precedes the SST anomalies by -20 days. If this “fit” is subtracted from the full \mathbf{map}_{lag} regression (M), the remaining pattern (M_r) is considered the “residual” portion of the regression that is not related to the “atmospheric forcing” at negative lags. Thus, the residual patterns are potentially related to ocean forcing of the atmosphere. This spatial linear decomposition into a “fit” and “residual” will help assert the independence of patterns seen at positive lags (lagging the ocean) from patterns seen at negative lags (leading the ocean).

2.4.3. Significance Testing

To determine the statistical significance of the regression patterns, correlation coefficients and the Student’s T-test were used to analyze the results. The correlation coefficient, r , provides a quantitative indication of the spread in the real data about the best fit line (and the square of r indicates the percent of variance of \mathbf{y} explained by the fit of $\hat{\mathbf{y}}$). It is defined by:

$$r = \frac{\overline{x'y'}}{\sigma_x \sigma_y} \quad (13)$$

or the covariance between x and y divided by the product of the standard deviations of x and y . Correlation coefficients were calculated at each grid point for all lags.

The Student’s t-Test was applied to the correlation maps to assess the statistical significance of the correlation coefficients between \mathbf{y} and $\hat{\mathbf{y}}$:

$$t = \frac{r\sqrt{N_{eff} - 2}}{\sqrt{1 - r^2}}. \quad (14)$$

The effective sample size (N_{eff}) is a conservative estimate of the independent samples for each variable: 1 degree of freedom per month for SST and 1 degree of freedom per 10 days for $v^*T_{850}^*$, Z_{1000} , and Z_{500} . The test was performed for a two-tailed 95% confidence level at each grid point within the region to determine if the correlation coefficient was significantly different from the null hypothesis of $r = 0$. Correlations that pass the Student's T-test are considered robust and differentiated from signals related to noise.

CHAPTER 3: RESULTS

3.1. North Pacific

3.1.1. K_{SST} Index

To identify relationships between atmospheric variability and variations in SST within the Kuroshio-Oyashio WBC region, monthly SST, $v^*T_{850}^*$, Z_{1000} , and Z_{500} are regressed onto the K_{SST} index for the DJF season over the North Pacific. Figure 3.1 illustrates the contemporaneous regressions of each variable, with SST, $v^*T_{850}^*$, and Z_{500} superposed on Z_{1000} contours. In Figure 3.1.a, it is evident that cold SST in the Kuroshio-Oyashio Extension region is associated with anomalously low geopotential height at the surface and anomalously warm SST along the west coast of North America. The SST anomalies shown are consistent

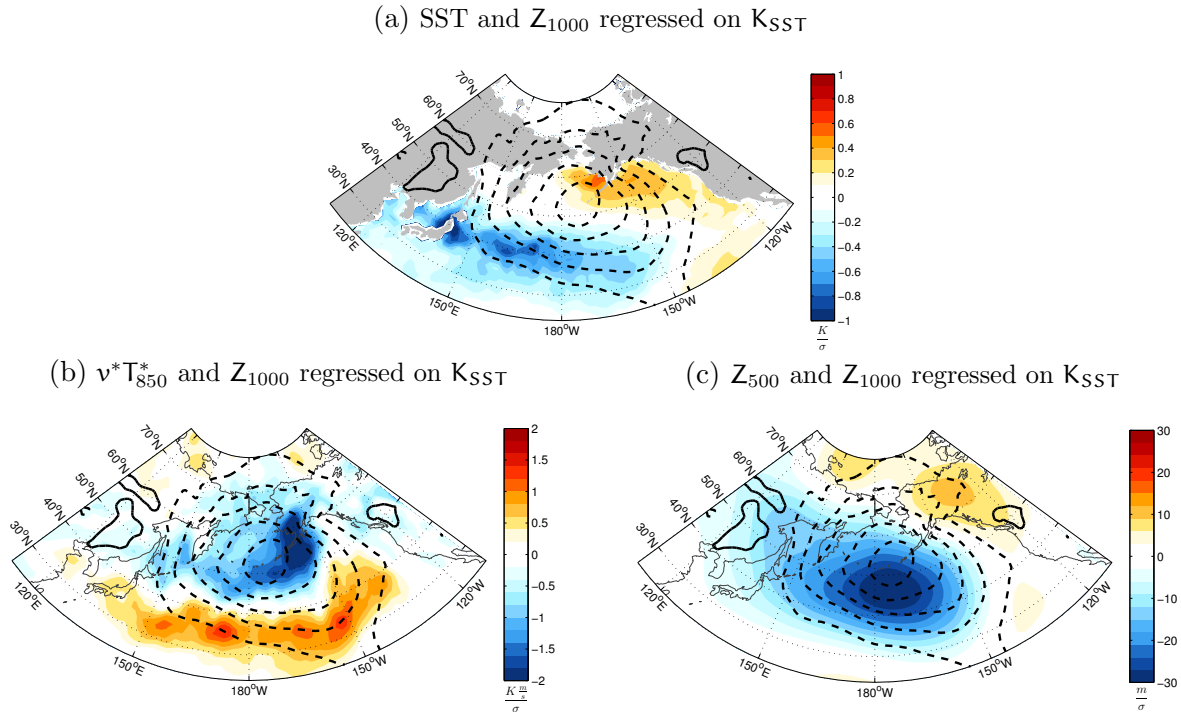


Figure 3.1. Contemporaneous DJF monthly regressions on K_{SST} for Z_{1000} (contours) and a) SST, b) $v^*T_{850}^*$, and c) Z_{500} (shading). Red (blue) shading indicates positive (negative) values, and solid (dashed) lines represent positive (negative) contours, with interval spacing of 4m between contours.

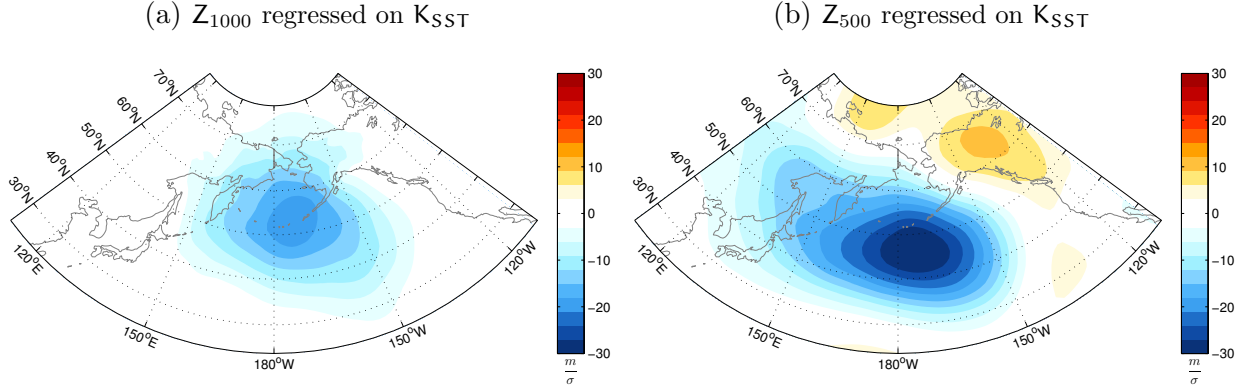


Figure 3.2. Same as in Fig. 3.1, except for a) Z_{1000} and b) Z_{500} regressed on K_{SST} .

with temperature advection by the anomalous surface circulation; regions of cold (warm) SST anomalies coincide with northerly (southerly) winds on the western (eastern) side of the surface low. The $\mathbf{v}^*T_{850}^*$ anomalies related to anomalously cold SST in Figure 3.1.b are positive along the southern edge of the surface low and negative near the center, with the strongest negative values around the Alaska Peninsula. It is of interest to note that the positive $\mathbf{v}^*T_{850}^*$ anomalies along the southern edge of the low are generally coincident with the region of high SST variability. At upper levels, there is also a low geopotential height anomaly at 500hPa located slightly to the south of the surface low, as illustrated in Figure 3.1.c. The relative strengths of the surface and 500hPa lows are depicted in Figure 3.2, and it is evident that the negative geopotential height anomalies become more intense with height, which is indicative of an equivalent barotropic low.

The monthly-mean observational results in Figure 3.1 confirm that extratropical SST anomalies are consistent with forcing by the atmosphere (as noted by Kushnir *et. al.* 2002 and authors therein). To investigate the possibility that a component of the regressions reflect ocean influence on the atmospheric circulation, we also performed daily lag regressions for each variable onto the K_{SST} index. The results are shown in Figure 3.3. Note that the contemporaneous regressions for daily data are slightly different from those for monthly-mean data (Figure 3.1). The K_{SST} index is fixed for the DJF time period, so patterns at negative lags represent SST, $\mathbf{v}^*T_{850}^*$, Z_{1000} , and Z_{500} leading the ocean, while the positive lag

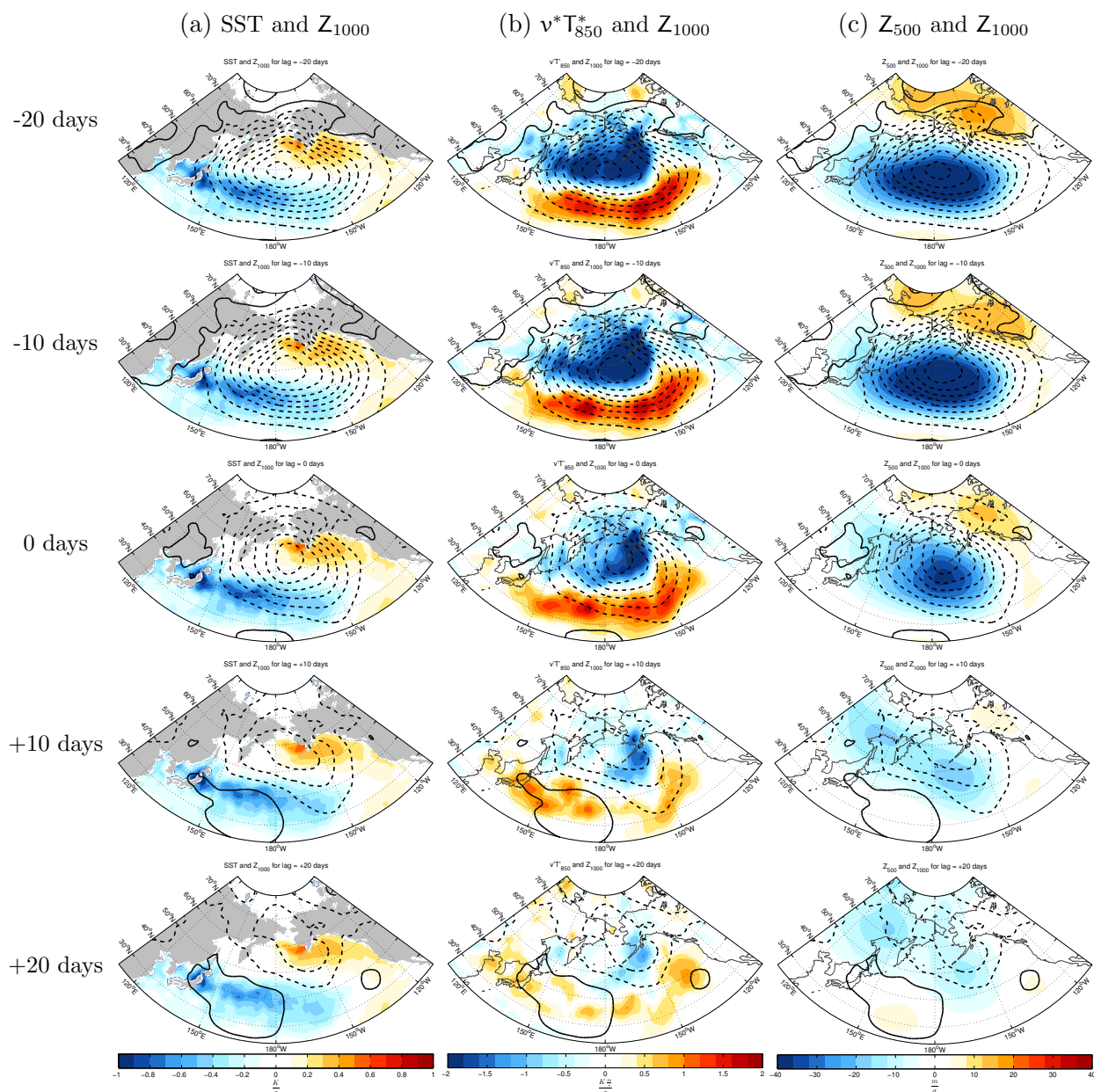


Figure 3.3. Lag regressions on K_{SST} for a) SST and Z_{1000} , b) $v^*T_{850}^*$ and Z_{1000} , and c) Z_{500} and Z_{1000} . Z_{1000} is shown in contours with solid (dashed) lines representing positive (negative) values at an interval spacing of 4 meters. Negative lags are indicative of the variables leading K_{SST} , and positive lags are indicative of K_{SST} leading the variables. Recall that the K_{SST} index is fixed for the DJF time period.

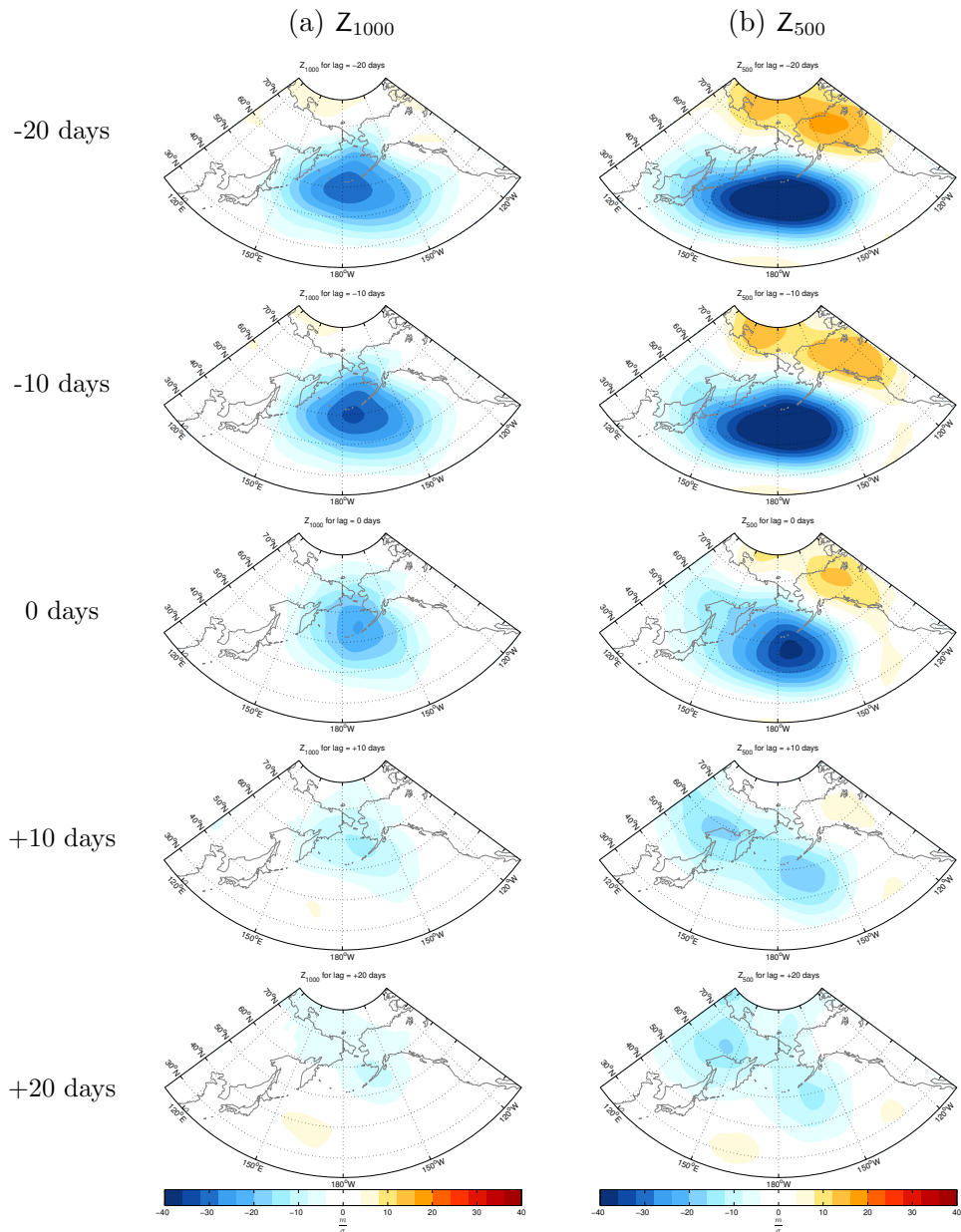


Figure 3.4. Same as in Figure 3.3, except for a) Z_{1000} and b) Z_{500} .

patterns represent the variables lagging the ocean. Figure 3.3.a shows that anomalously cold SST remains relatively unchanged between negative and positive lags, with some decay in magnitude towards positive lag. The Z_{1000} field indicates a strong surface low geopotential height anomaly preceding the ocean at least 20 days prior and a geopotential height dipole at positive lags, with a low centered over anomalously warm SST near Alaska and a weaker high located over anomalously cold SST in the Kuroshio-Oyashio Extension region. In Figure 3.3.b, it is evident from lags of -20 and -10-days that $v^*T_{850}^*$ along the southern side of the negative geopotential height anomaly is associated more with the presence of the surface low rather than anomalously cold SST; the eddy heat flux signal appears to dissipate by +20-days. The upper level low geopotential height anomaly seen in Figure 3.3.c is strongest at a lag of -20-days, with a weaker low (high) above the remaining surface low (high) at positive lags. A second 500hPa below-average geopotential height anomaly is present over northeastern Russia at the +10 and +20-day lags. The relative strength of geopotential height anomalies at the surface and 500hPa is shown in Figure 3.4. The comparison indicates that the upper level low is more intense than the surface at all lags except at +20-days. At this lag, the 500hPa low is only slightly stronger than the surface low directly below, and the high is of similar strength between the two levels.

To further investigate the patterns present at positive lags, a spatial linear decomposition was performed on the lag regressions of each variable, as described in the methods. Figures 3.5-7 show the spatial decompositions, where the full lag regression (a) is equal to the sum of the fit (b) and residual (c), as described in Chapter 2. By construction, the residual values at -20-days are equal to zero at all grid boxes. The residual lag regressions make clear signals in the regressions at positive lags that are independent of the -20-day pattern. Recall that the “fit to map_{-20} ” can be interpreted as the atmosphere forcing the ocean while the “residual” can be considered the atmospheric “response”.

The SST decompositions in Figure 3.5 indicate that the SST patterns do not vary much from the -20-day lag regression map, which is expected as the ocean has a large heat

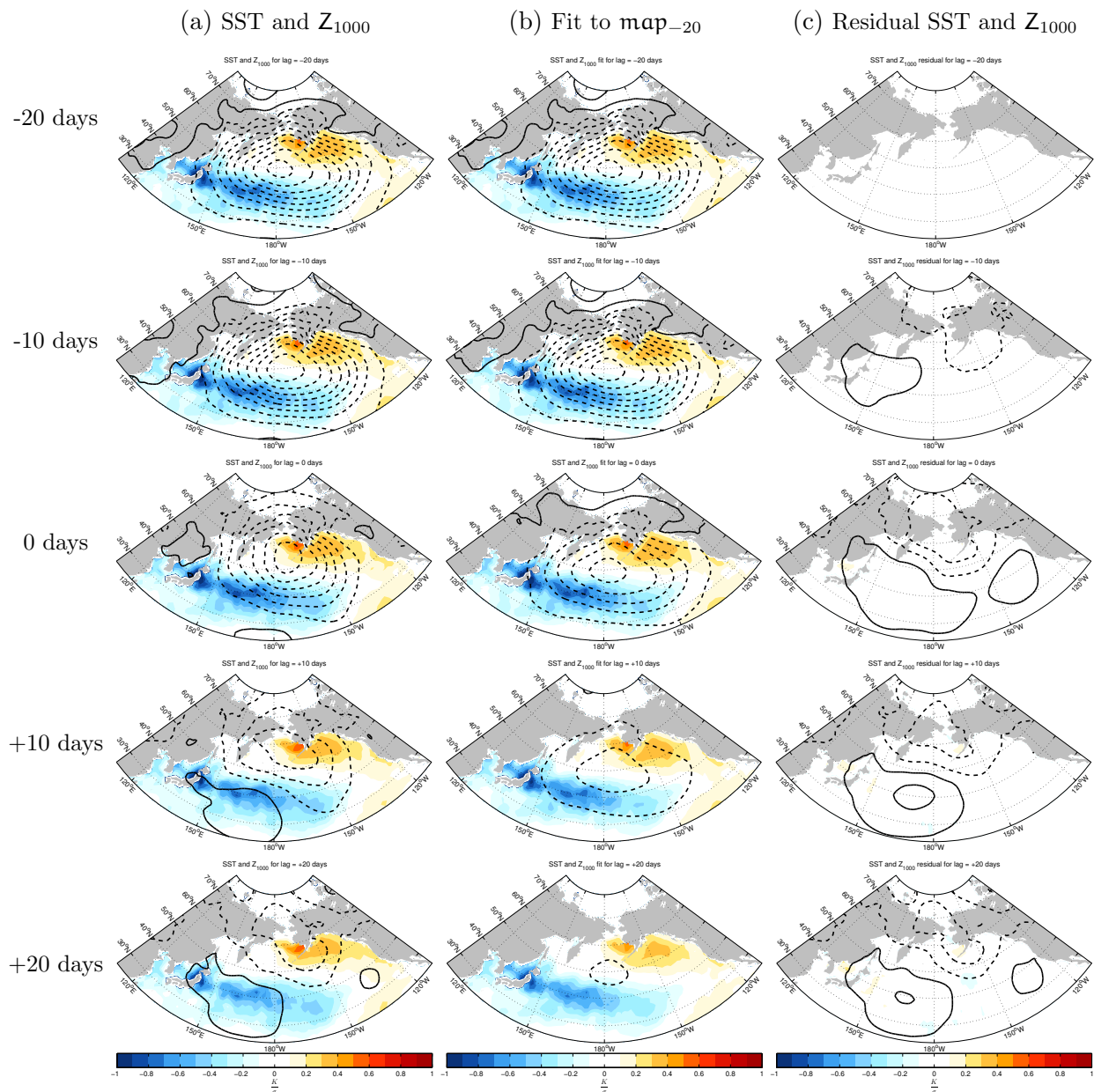


Figure 3.5 Linear decomposition of SST (shading) and Z₁₀₀₀ (contours) with a) the full SST and Z₁₀₀₀ regression on K_{SST} at each lag, b) the linear fit of SST and Z₁₀₀₀ to the full -20-day lag regression, and c) the residual SST and Z₁₀₀₀ at each respective lag. Note that at each lag, $map_A = map_B + map_C$.

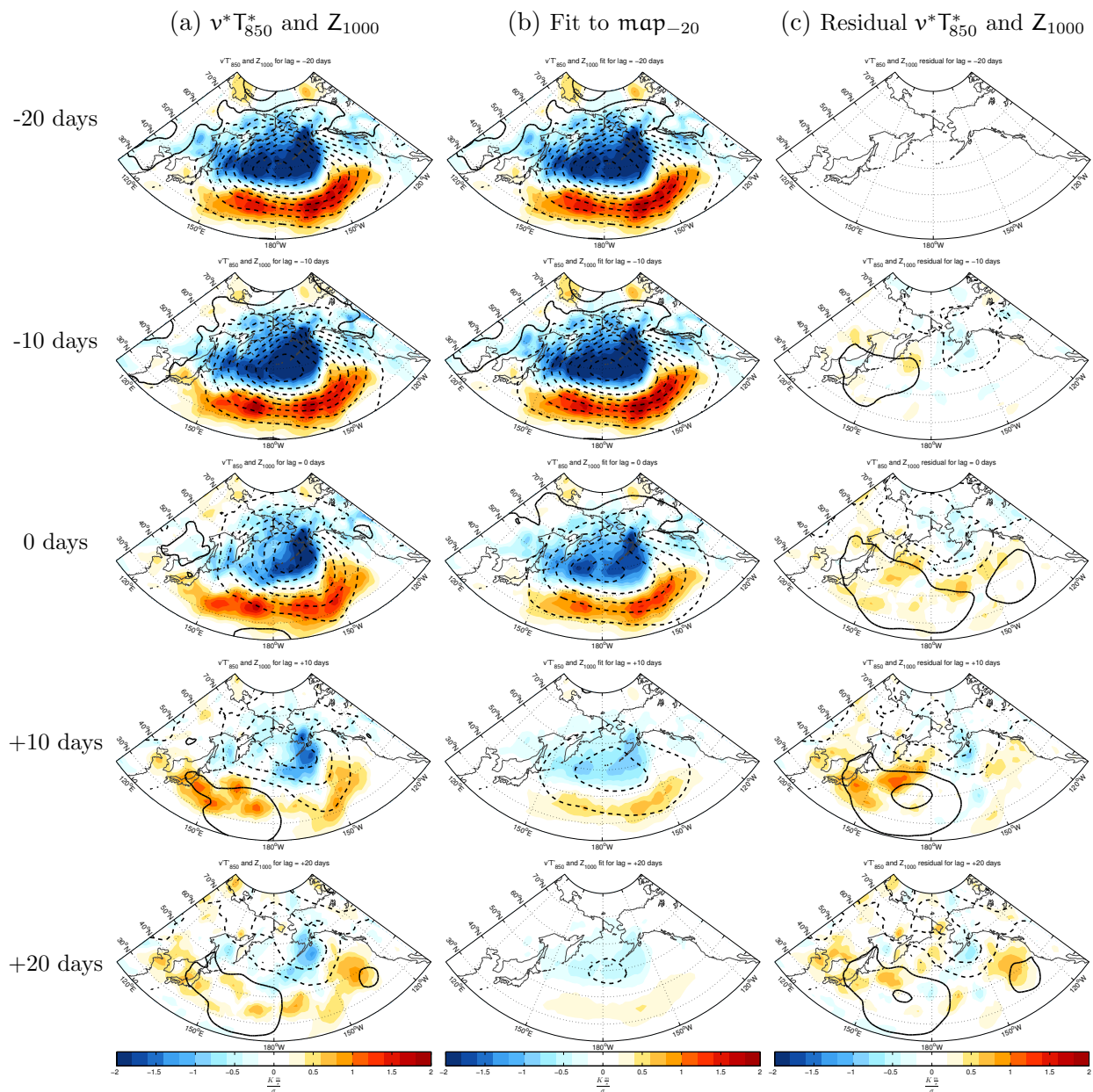


Figure 3.6 Same as in Figure 3.5 except linear decomposition of $v^*T_{850}^*$ (shading) and Z_{1000} (contours).

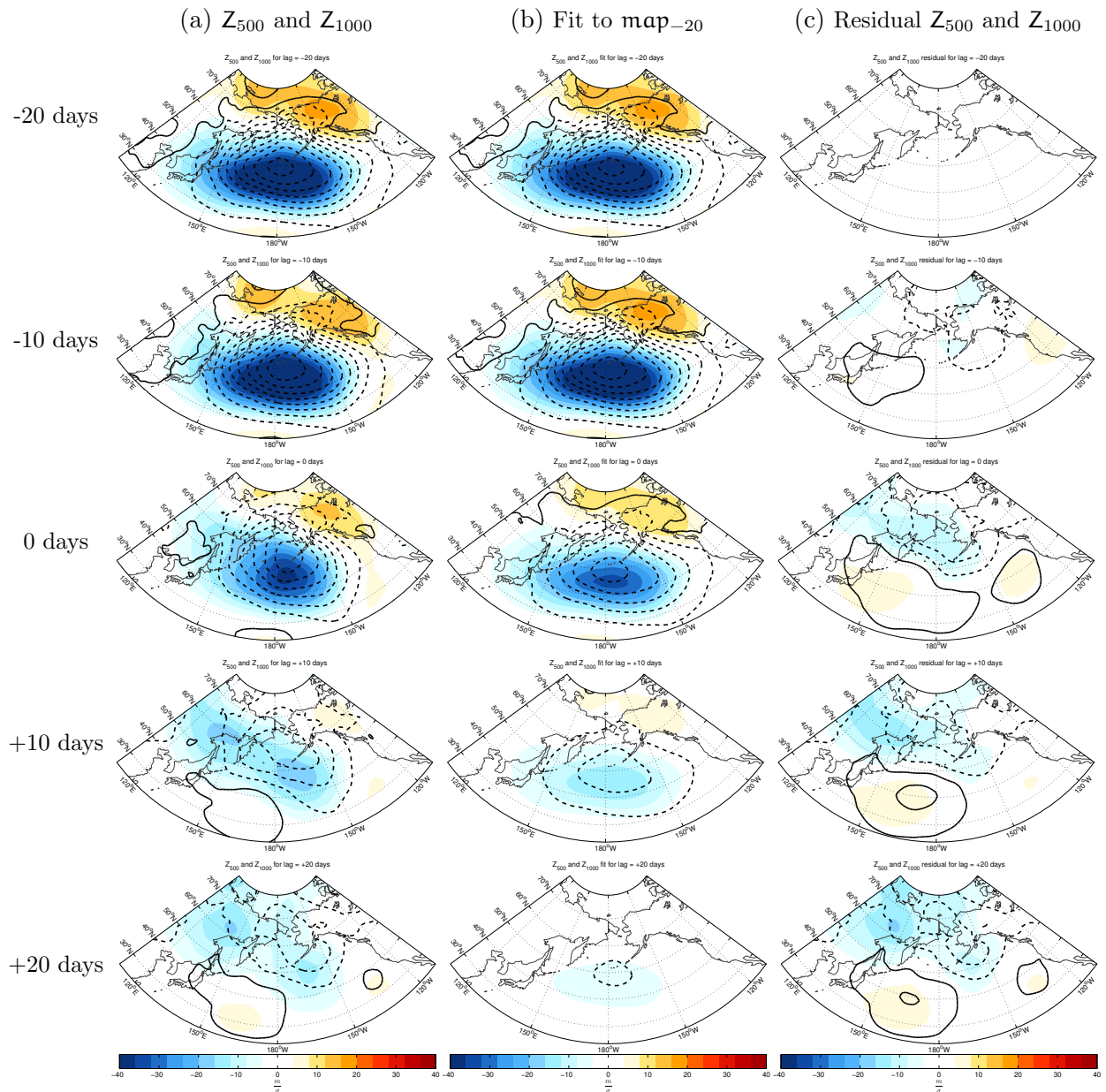


Figure 3.7 Same as in Figure 3.5 except linear decomposition of Z_{500} (shading) and Z_{1000} (contours).

capacity. As for the Z_{1000} field, the geopotential height dipole at positive lags appears unrelated to the negative geopotential height anomaly pattern at -20-days. It is evident from the “fit” in the middle column that a component of the Z_{1000} -20-day pattern is present at each subsequent lag; the signal decays and almost disappears by a lag of +20-days. A similar decay is present in the $v^*T_{850}^*$ and Z_{500} fields in Figures 3.6-7.

Hence the monthly-mean regressions onto K_{SST} (Figure 3.1) can be viewed as the superposition of two distinct patterns: 1) a pattern that peaks 2-3 weeks before the SST anomaly and is consistent with forcing of the ocean (*e.g.*, Figure 3.5.b) and 2) a pattern that peaks after the SST anomaly (*e.g.*, Figure 3.5.c). The results reveal that the first pattern (“the atmosphere forcing the ocean”) decays in time while the second pattern (“the atmospheric response”) grows in time, as shown in the middle and right columns of Figures 3.5-7, respectively. With the “atmospheric forcing” removed from the full lag regression, the remaining pattern, or the “atmospheric response”, indicates a potential relationship to ocean forcing.

The significance of the key features in Figure 3.5 is tested as follows. The Student’s T-test is applied to the correlation maps of SST and Z_{1000} at all lags, as described in the methods. Stippling shown in Figure 3.8 indicates results that exceed the 95% confidence level. In the first column, the negative SST correlations are high and significant around the Kuroshio-Oyashio Extension region; the high significance is expected as the SST field does not vary greatly from negative to positive lags. The positive SST correlations along the western coast of North America are also significant. In the second column, the negative Z_{1000} correlations indicate that the surface low is significant at negative lags. While the weakened low at a lag of zero days is still significant, neither the negative nor positive geopotential height anomalies are significant at positive lags.

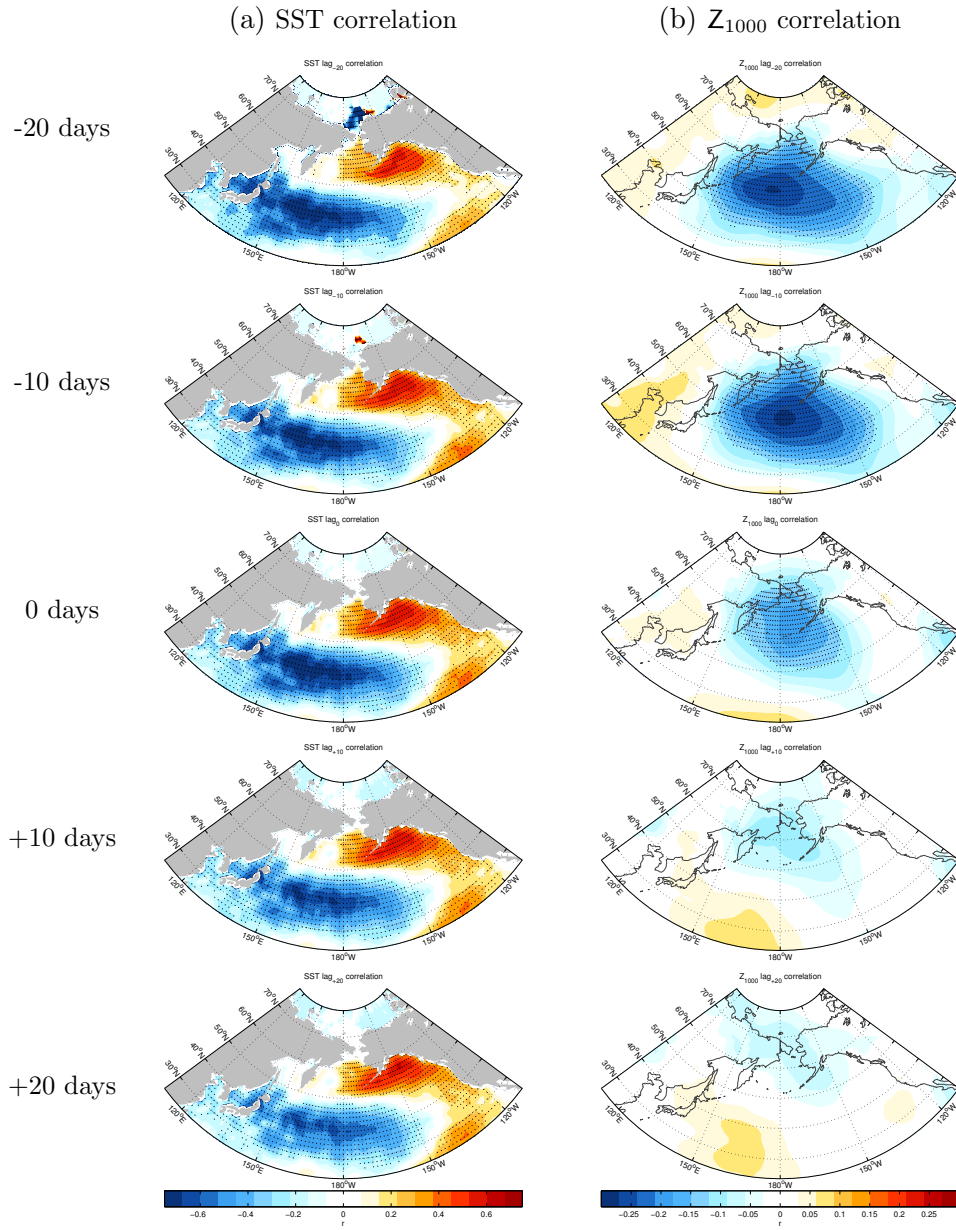


Figure 3.8 Correlations for a) SST and b) Z_{1000} on K_{SST} at all lags. Stippling indicates significance at the 2-tailed 95% confidence level.

3.1.2. PNA Index

To complement the analysis in the previous section, we will consider an atmospheric index in addition to the SST index. The K_{SST} index provided an assessment of how the atmospheric circulation lags variability in SST near the WBC. Now, the use of an atmospheric index allows us to determine if significant SST patterns precede changes in the leading mode of atmospheric variability in the North Pacific. Here we test the robustness of the key results in the previous section in analysis based not on SST variability in the Kuroshio-Oyashio Extension region, but on a time series of the Pacific/North American Pattern (PNA).

The PNA index is defined as the second EOF of monthly-mean SLP anomalies over the winter season [*e.g.*, Quadrelli and Wallace 2004]. To obtain a daily-resolution time series for the PNA index, EOF2 was projected onto the cosine-weighted daily SLP anomalies. The characteristic Z_{500} pattern associated with the PNA is depicted in Figure 3.9 for reference. The positive phase of the PNA is associated with above-average heights over North America and below-average heights south of the Aleutian Islands and over the southeastern United States [*e.g.*, Wallace and Gutzler 1980; Quadrelli and Wallace 2004]. Negative geopotential height anomalies are also present over the North Atlantic [*e.g.*, Wallace and Thompson 2002].

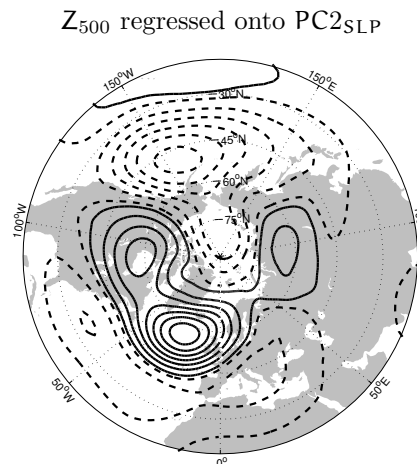


Figure 3.9 Contemporaneous monthly Z_{500} regressed on the PNA index, or the second principal component of SLP. Solid (dashed) lines indicate positive (negative) contours with 10 meter interval spacing.

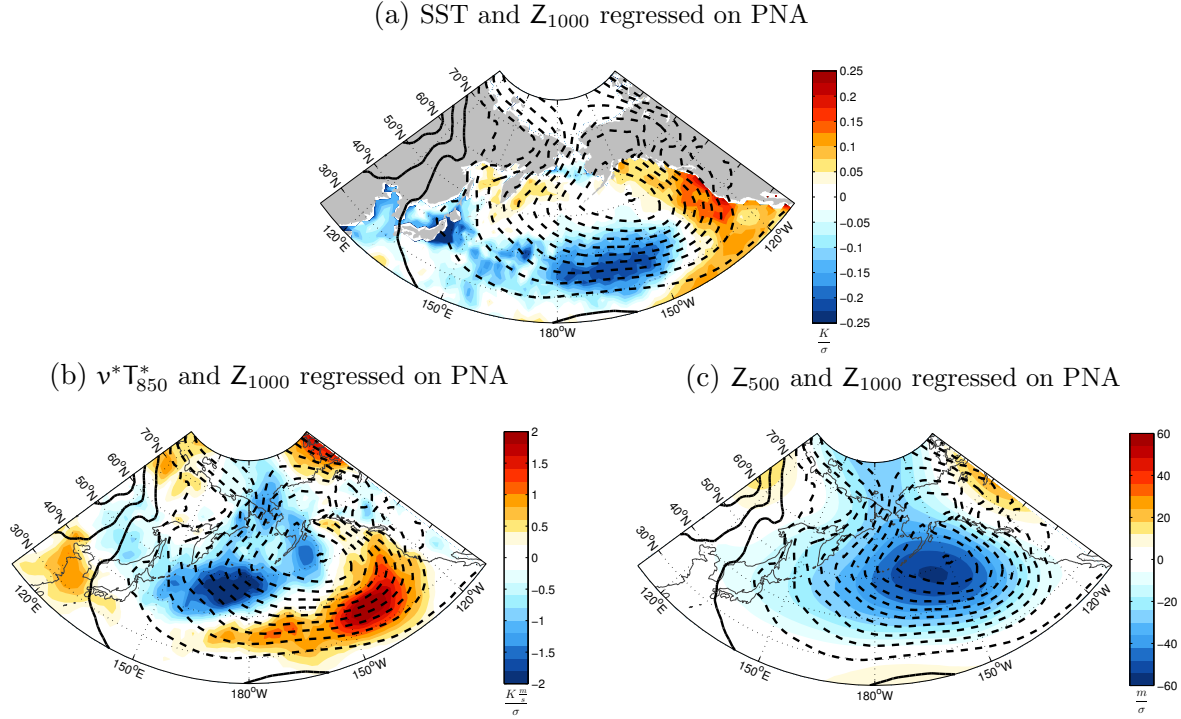


Figure 3.10. Contemporaneous DJF monthly regressions on the PNA for Z_{1000} (contours) and a) SST, b) $v^*T_{850}^*$, and c) Z_{500} (shading). Red (blue) shading indicates positive (negative) values, and solid (dashed) lines represent positive (negative) contours, with interval spacing of 4 meters between contours. Note that the SST and Z_{500} colorbars have different ranges compared to Figure 3.1.

The strong negative geopotential height anomaly at the 500hPa level over the North Pacific appears similar to the pattern associated with the K_{SST} index (compare Figures 3.1 and 3.9). The analysis is repeated for the PNA to assess the similarities and differences in the results between the two indices. Note that, for the atmospheric index, negative lags now denote the ocean leading the atmosphere (when considering SST) and vice versa for positive lags.

Figure 3.10 shows the monthly-mean contemporaneous regressions of SST, $v^*T_{850}^*$, Z_{1000} , and Z_{500} on standardized values of the PNA index. The PNA is associated with anomalously low Z_{1000} over the North Pacific sector that are reminiscent of those associated with the K_{SST} index (Figure 3.1). Again, the negative geopotential height anomalies increase in strength with height and are located above and slightly to the south of the surface low, as indicated in Figures 3.10.c and 3.11. The strengths of the surface and upper level lows are roughly double of those derived from regressions onto the K_{SST} index. The SST fields

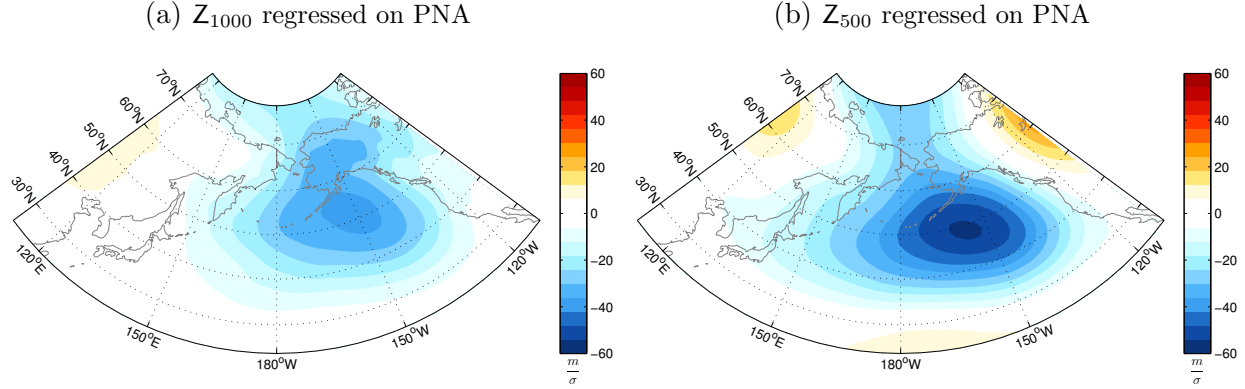


Figure 3.11. Same as in Fig. 3.10, except for a) Z_{1000} and b) Z_{500} regressed on the PNA.

associated with the PNA and K_{SST} indices display similar patterns of cold SST anomalies along the Kuroshio-Oyashio Extension and warm SST anomalies along the west coast of North America. However, the amplitudes are weaker compared to those regressed on K_{SST} , and there is a more pronounced SST signal around the subtropical front/ENSO teleconnection region [*e.g.*, Nakamura *et. al.* 1997; Diaz *et. al.* 2001 and authors therein]. As for $\mathbf{v}^*T_{850}^*$, the PNA pattern is different from the K_{SST} pattern; negative $\mathbf{v}^*T_{850}^*$ anomalies occur where northerly advection is present in the surface low, and positive anomalies occur where southwesterly advection is present. Despite the noticeable differences, the similarities in SST and geopotential height indicate some connection between the atmosphere and ocean indices (K_{SST} and the PNA are correlated at $r = -0.2$ on monthly-mean timescales).

To further contrast the oceanic and atmospheric signatures of the PNA with K_{SST} , lag regressions were also performed on the PNA index, as seen in Figure 3.12. It appears that atmospheric forcing is responsible for the weaker patterns at negative lags while positive lags indicate damped signals of the PNA pattern. Consistent with results from Deser and Timlin [1997], robust SST anomalies occur approximately 2-3 weeks after the peak in the PNA. There is also a noticeable resemblance between the +10-day PNA lag pattern in Figure 3.12 and the 0-day and negative K_{SST} lag regressions shown in Figures 3.1 and 3.3. However, the lack of a strong SST signal prior to the onset of the PNA suggests that the midlatitude ocean is not responsible for forcing the atmospheric variability in the North Pacific.

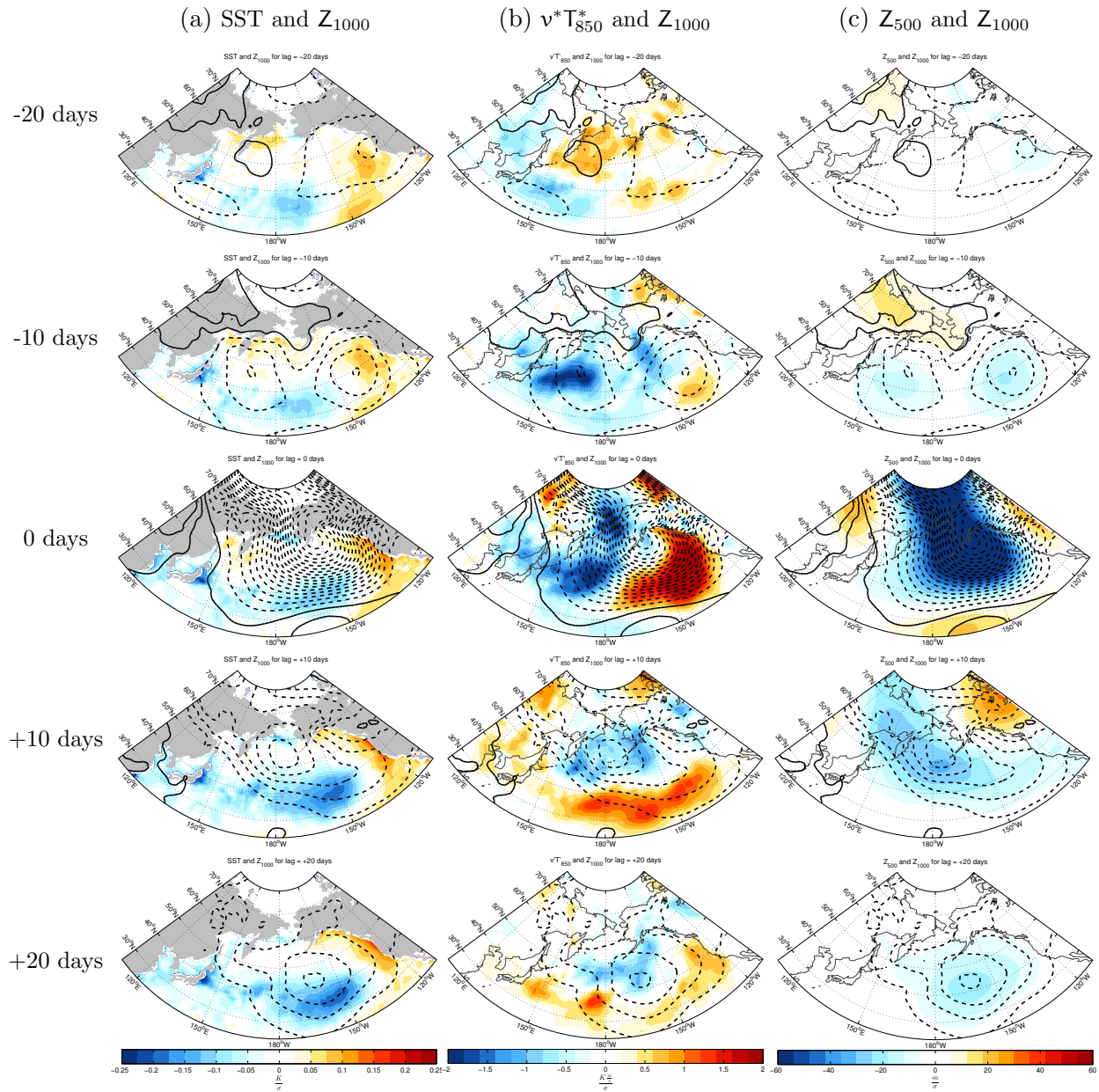


Figure 3.12 Lag regressions on the PNA for a) SST and Z_{1000} , b) $v^*T_{850}^*$ and Z_{1000} , and c) Z_{500} and Z_{1000} . Z_{1000} is shown in contours with solid (dashed) lines representing positive (negative) values at an interval spacing of 4 meters. Negative lags are indicative of the variables leading PNA, and positive lags are indicative of PNA leading the variables. Recall that the PNA index is fixed for the DJF time period.

3.2. North Atlantic

3.2.1. G_{SST} Index

Here we repeat the analysis in the previous section for the North Atlantic region. Again, the goal of the analysis is to assess the lagged covariability between atmospheric and oceanic variability on weekly timescales and, specifically, to determine whether there are coherent patterns in the SST field that lead the atmosphere. Figure 3.13 shows monthly-mean regressions of SST, $v^*T_{850}^*$, Z_{1000} , and Z_{500} onto the G_{SST} index for the DJF season. As is the case over the North Pacific (Figure 3.1), anomalously cold SST coincides with below-average geopotential height at the surface centered to the northeast of the SST anomalies. Positive $v^*T_{850}^*$ anomalies are present to the south and east of the negative SST anomalies, with negative $v^*T_{850}^*$ anomalies located to the north. An upper level low is also apparent at 500hPa and stacked slightly southwest of the anomalous surface low. Figure 3.14 confirms

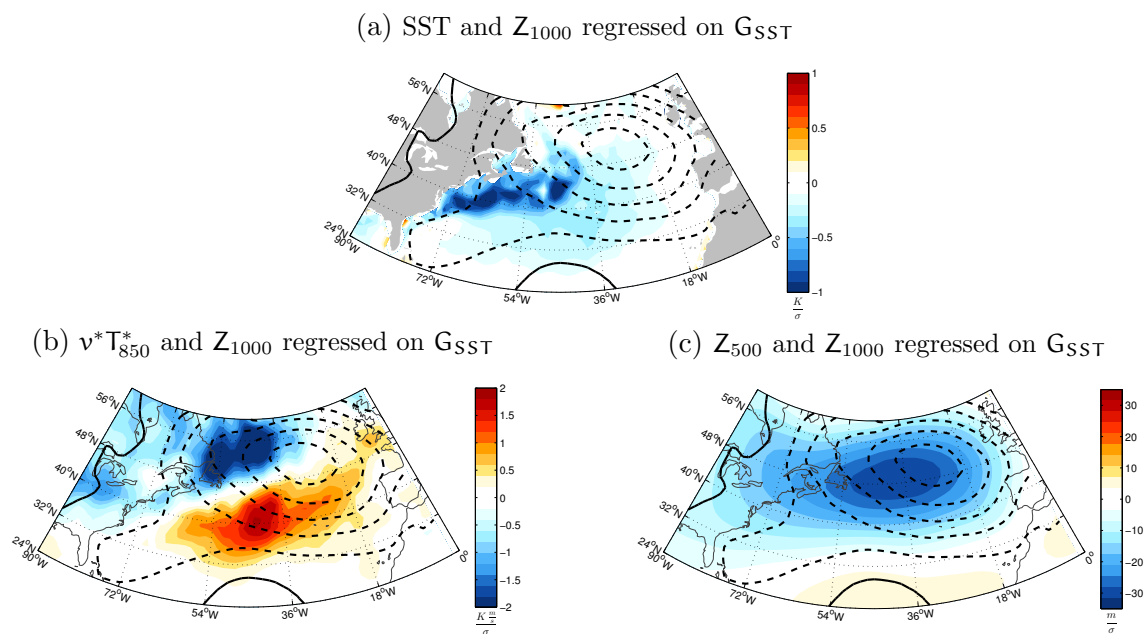


Figure 3.13. Contemporaneous DJF monthly regressions on G_{SST} for Z_{1000} (contours) and a) SST, b) $v^*T_{850}^*$, and c) Z_{500} (shading). Red (blue) shading indicates positive (negative) values, and solid (dashed) lines represent positive (negative) contours, with interval spacing of 4 meters between contours.

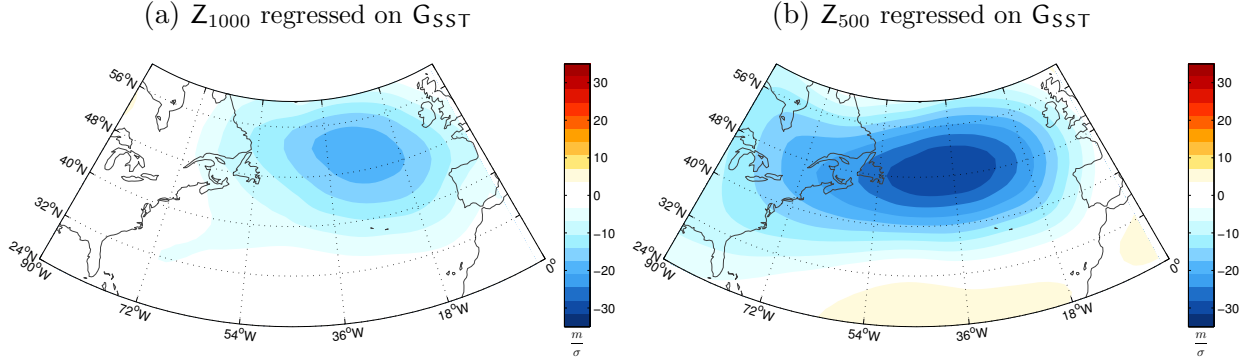


Figure 3.14. Same as in Fig. 3.13, except for a) Z_{1000} and b) Z_{500} regressed on G_{SST} .

that the negative Z_{500} anomalies are stronger than the Z_{1000} anomalies, indicating a low that deepens with height.

Lag regressions based on daily values of the same fields and the G_{SST} index are shown in Figure 3.15. At first glance, there appears to be a more distinct difference between the atmospheric fields at negative and positive lags compared to similar analyses computed for the North Pacific (Figure 3.3). From the results at negative lag in Figure 3.15.a, it is clear that a strong negative geopotential height anomaly at the surface precedes changes in the SST field. Anomalously cold SSTs over the Gulf Stream region are consistent with cold air advection due to northerly flow over northeastern North America. The cold SST anomaly persists into positive lags, with some decay in amplitude. Note that the region of warm air advection on the eastern side of the low does not clearly lead to anomalously warm SST off the western coast of Europe. This result is consistent with the presence of weaker north-south gradients in SST on the eastern side of the Atlantic basin compared to the western side (Figure 2.1.d).

At positive lags (bottom panels in column a), a weak high emerges over the Western North Atlantic around +10-days and strengthens by +20-days, with what appears to be the remnants of the low to the north. The $\mathbf{v}^*T_{850}^*$ pattern at a lag of zero days is most pronounced at negative lags and appears to be associated with the surface low, as seen in Figure 3.15.b. While the signal in the eddy heat fluxes seems to decay by +10-days, a new region of positive

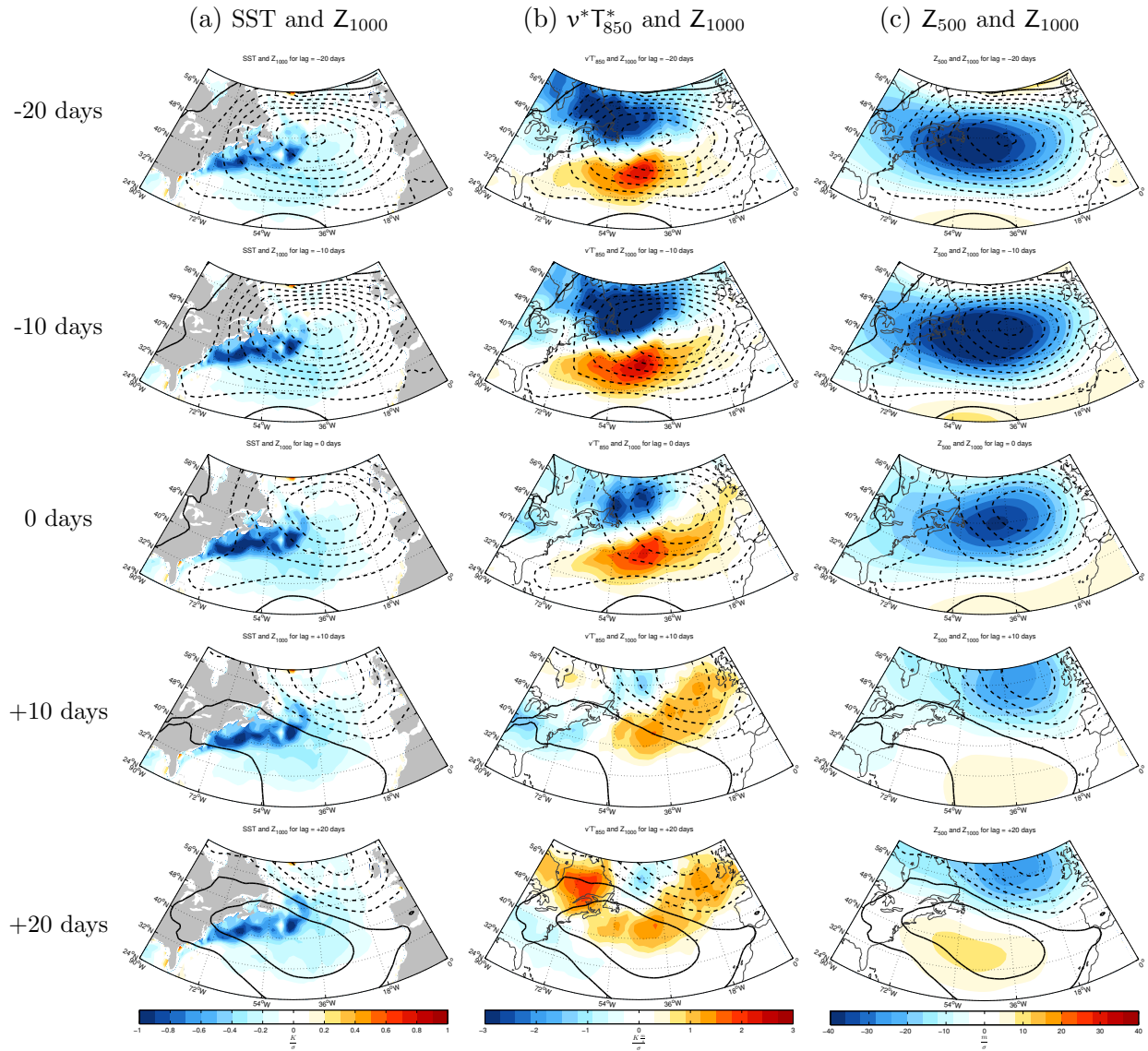


Figure 3.15 Lag regressions on G_{SST} for a) SST and Z_{1000} , b) $v^*T_{850}^*$ and Z_{1000} , and c) Z_{500} and Z_{1000} . Z_{1000} is shown in contours with solid (dashed) lines representing positive (negative) values at an interval spacing of 4 meters. Negative lags are indicative of the variables leading G_{SST} , and positive lags are indicative of G_{SST} leading the variables. Recall that the G_{SST} index is fixed for the DJF time period.

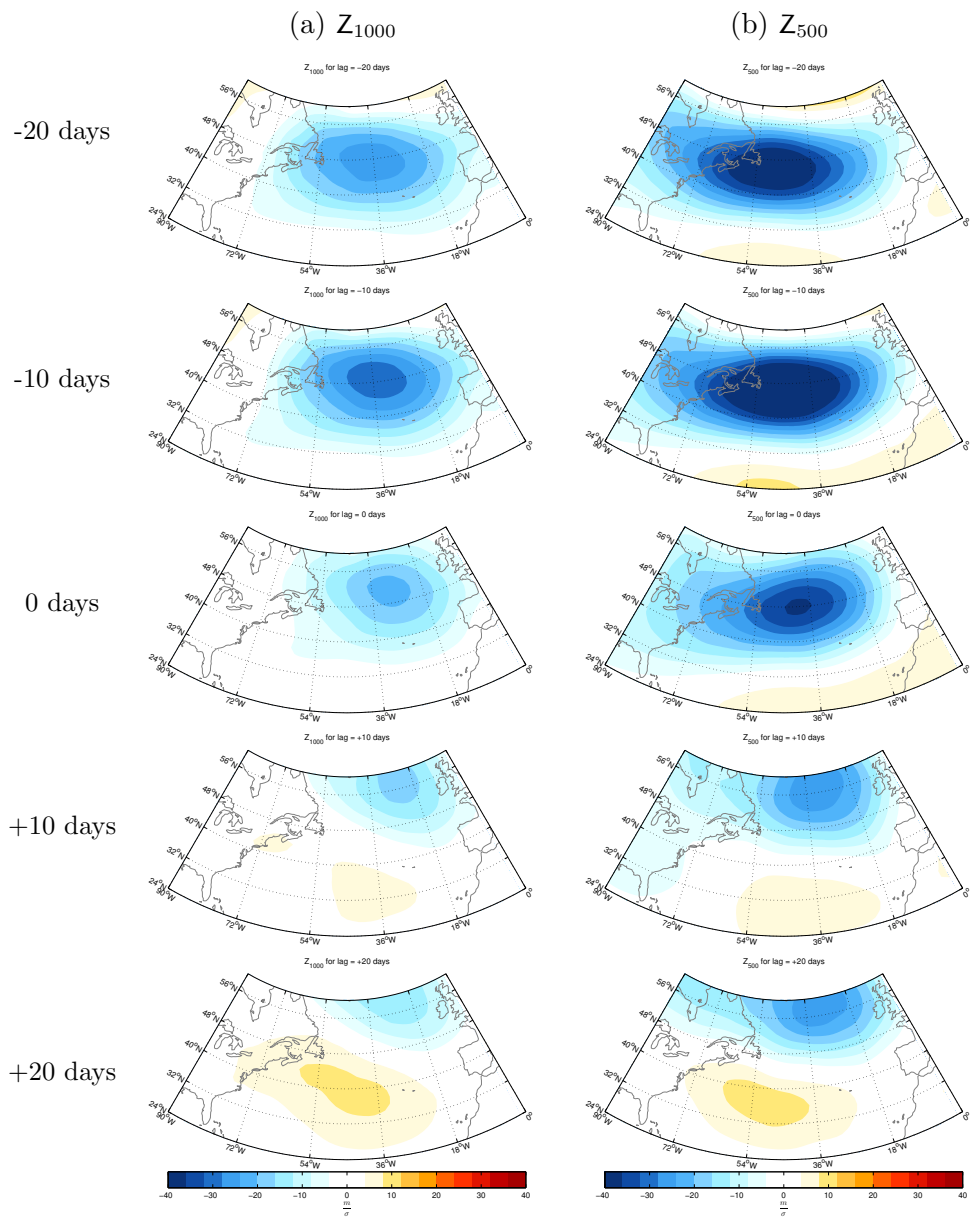


Figure 3.16 Same as in Figure 3.15, except for a) Z_{1000} and b) Z_{500} .

$v^*T_{850}^*$ anomalies build into northeastern Canada by +20-days. The Z_{500} anomalies follow a similar pattern as those at the surface. Figures 3.15.c and 3.16 reveal that the low deepens and is stacked with height slightly to the southwest through all lags. The positive geopotential height anomalies at positive lag similarly appear to stack with height towards the southwest, and the surface and upper-level high are of similar strength.

As done for the North Pacific sector (Figures 3.5-7), spatial linear decomposition is again conducted to help interpret the results of the regressions at positive lag (Figure 3.15). In general, the results at positive lags over the North Atlantic are more robust than those over the North Pacific. The SST anomalies do not notably change between negative and positive lags. Thus, the residual SST anomalies are very small at all lags (Figure 3.17). On the other hand, the residual Z_{1000} anomalies exhibit a distinct pattern at positive lags that grows with amplitude through +20-day lag. By construction, the residual geopotential height anomalies at positive lags are orthogonal to those that drive the SST anomalies in the first place. Similarly, the positive $v^*T_{850}^*$ anomalies extending from northeastern Canada into western Europe are orthogonal to the $v^*T_{850}^*$ anomalies at -20-day lag. The residual Z_{500} anomalies (Figure 3.19) suggest that the pattern of Z_{1000} anomalies at positive lag extend through the depth of the troposphere.

As is the case over the North Pacific, the monthly-mean regressions on G_{SST} (Figure 3.13) can be thought of as the superposition of two patterns. The middle column of Figure 3.17 (“the atmosphere forcing the ocean”) indicates a decaying pattern of the anomalous low at a lag of -20 days. The right column (“the atmospheric response”) shows a growing geopotential dipole pattern, with a high building over the region of cold SST anomalies. Again, after separating the “atmospheric forcing” (i.e., the -20-day lag map) from lag regressions, the residual signals reflect that component of the results that is linearly independent of the “atmospheric forcing” pattern.

The Student’s T-test was performed on the lag correlations of SST and Z_{1000} at all lags to determine the significance of the results. The SST patterns show significant negative

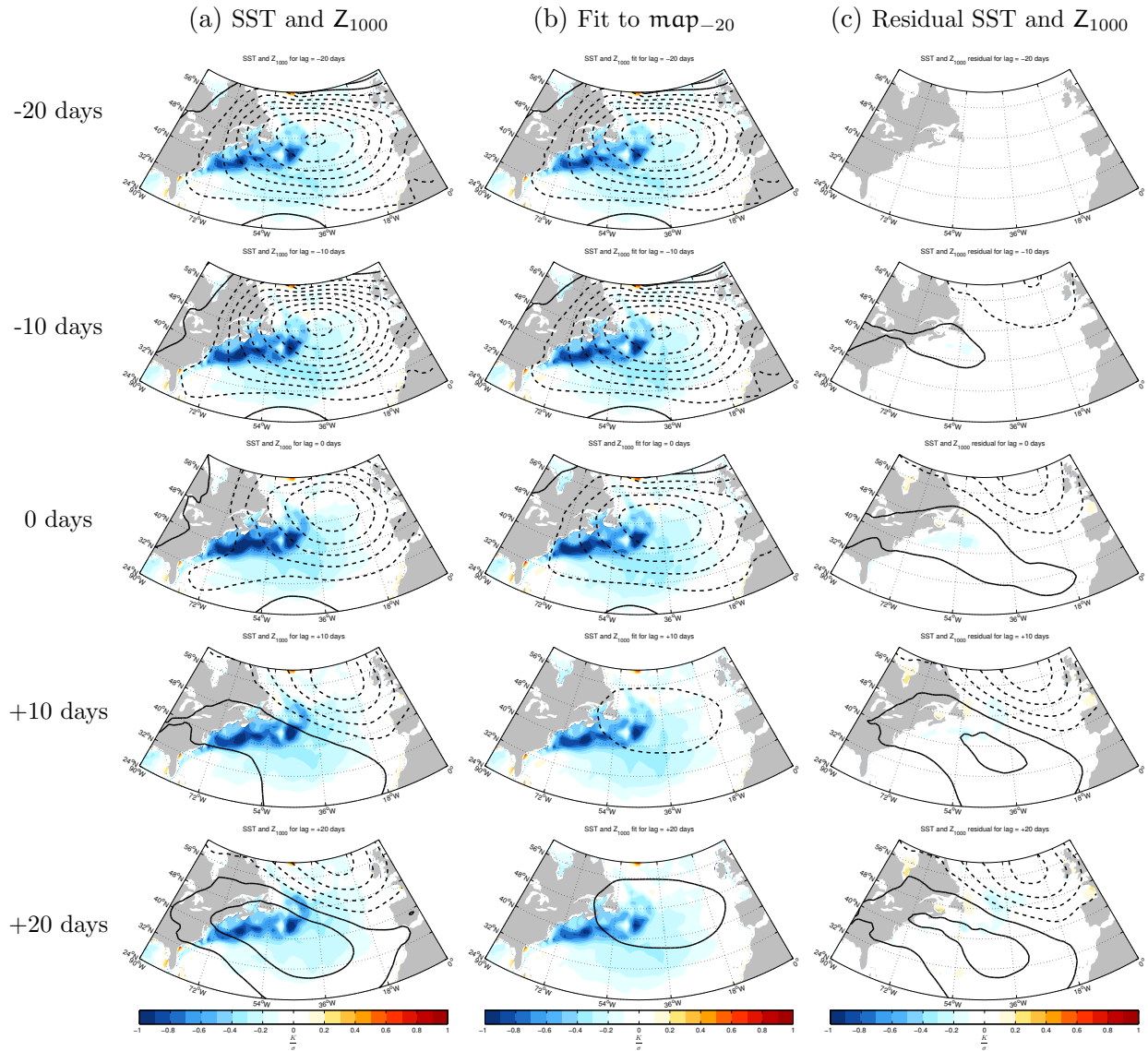


Figure 3.17 Linear decomposition of SST (shading) and Z_{1000} (contours) with a) the full SST and Z_{1000} regression on G_{SST} at each lag, b) the linear fit of SST and Z_{1000} to the full -20-day lag regression, and c) the residual SST and Z_{1000} at each respective lag. Note that at each lag, $map_A = map_B + map_C$.

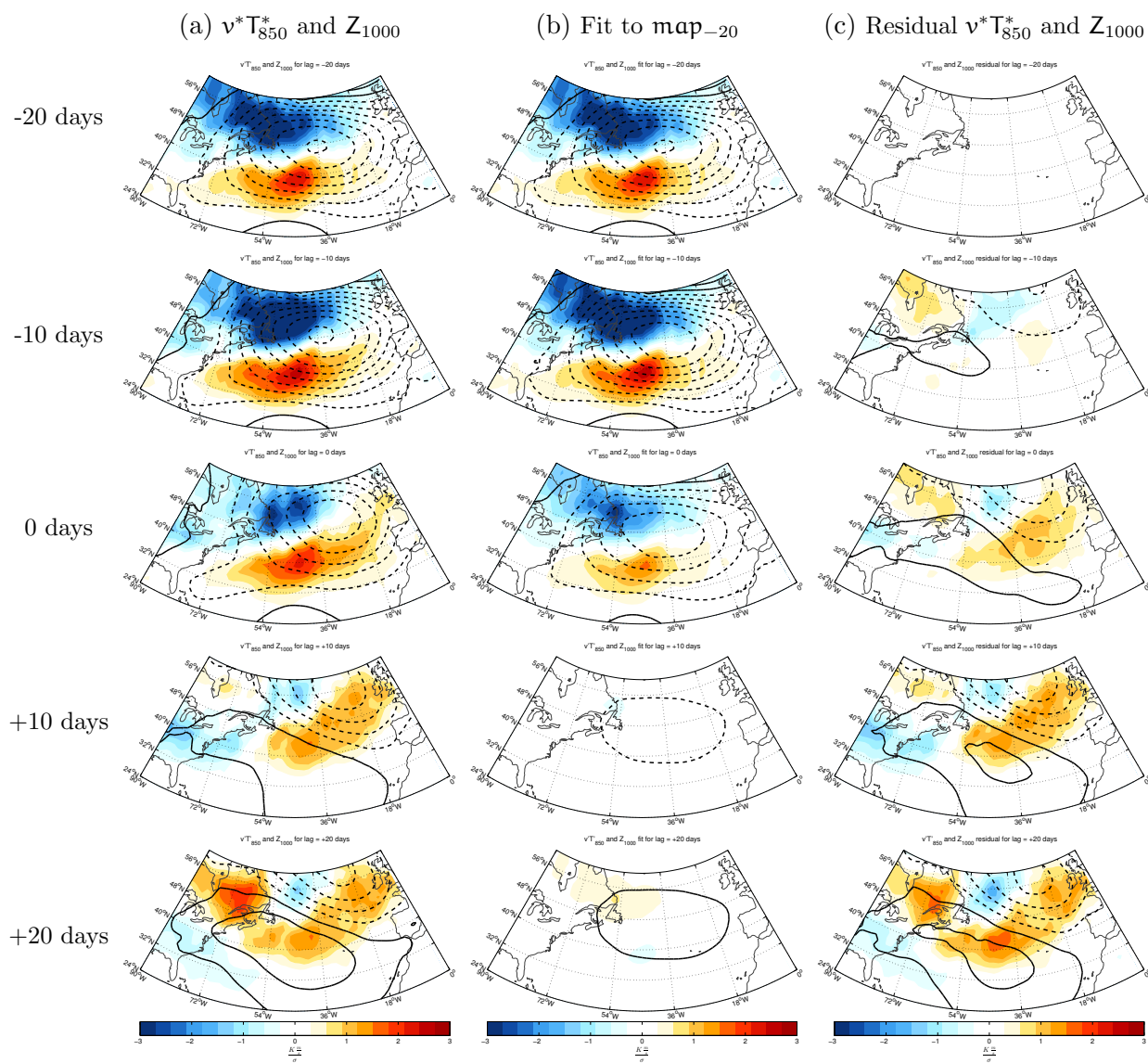


Figure 3.18 Same as in Figure 3.17 except linear decomposition of $v^*T_{850}^*$ (shading) and Z_{1000} (contours).

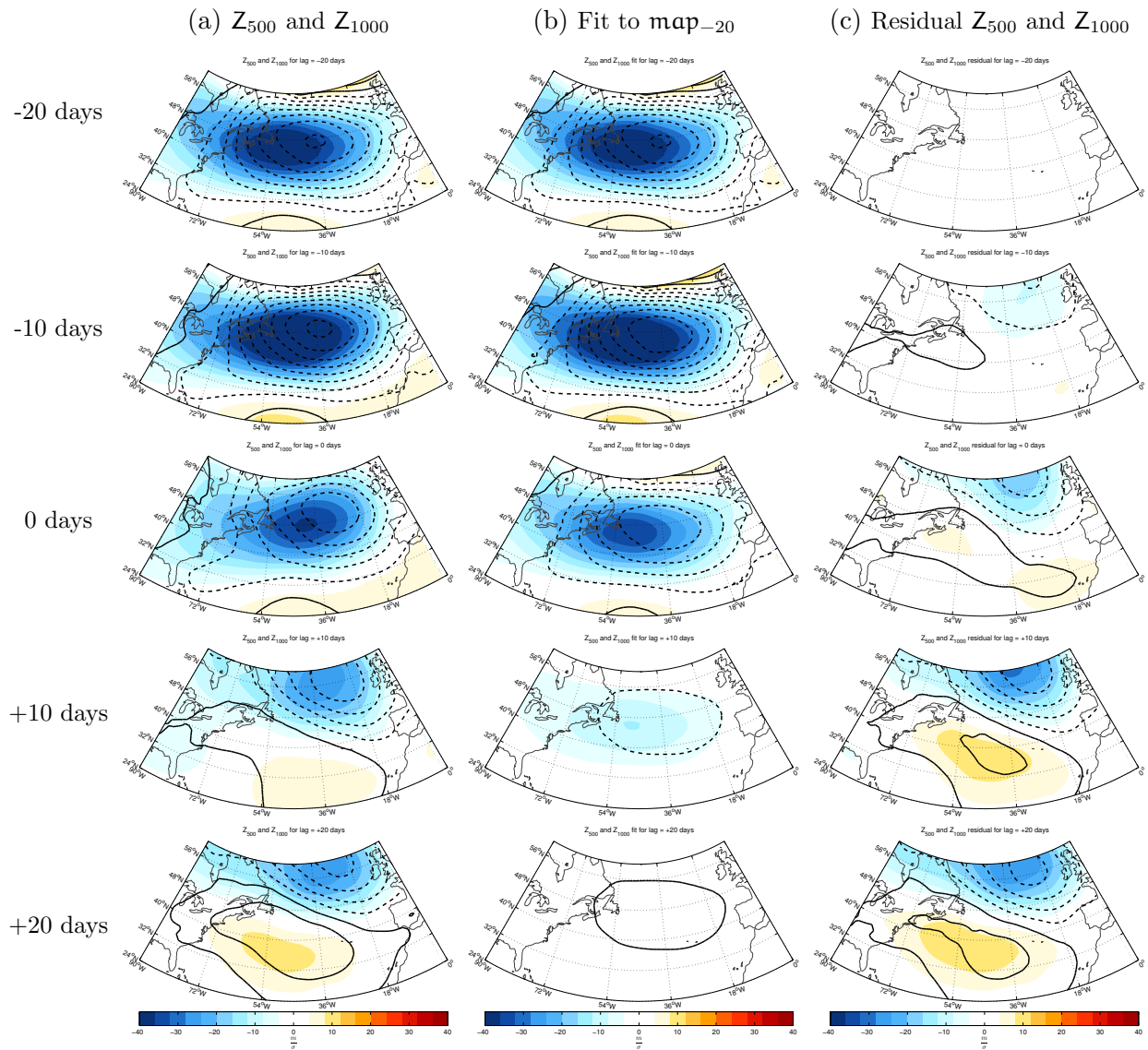


Figure 3.19 Same as in Figure 3.17 except linear decomposition of Z_{500} (shading) and Z_{1000} (contours).

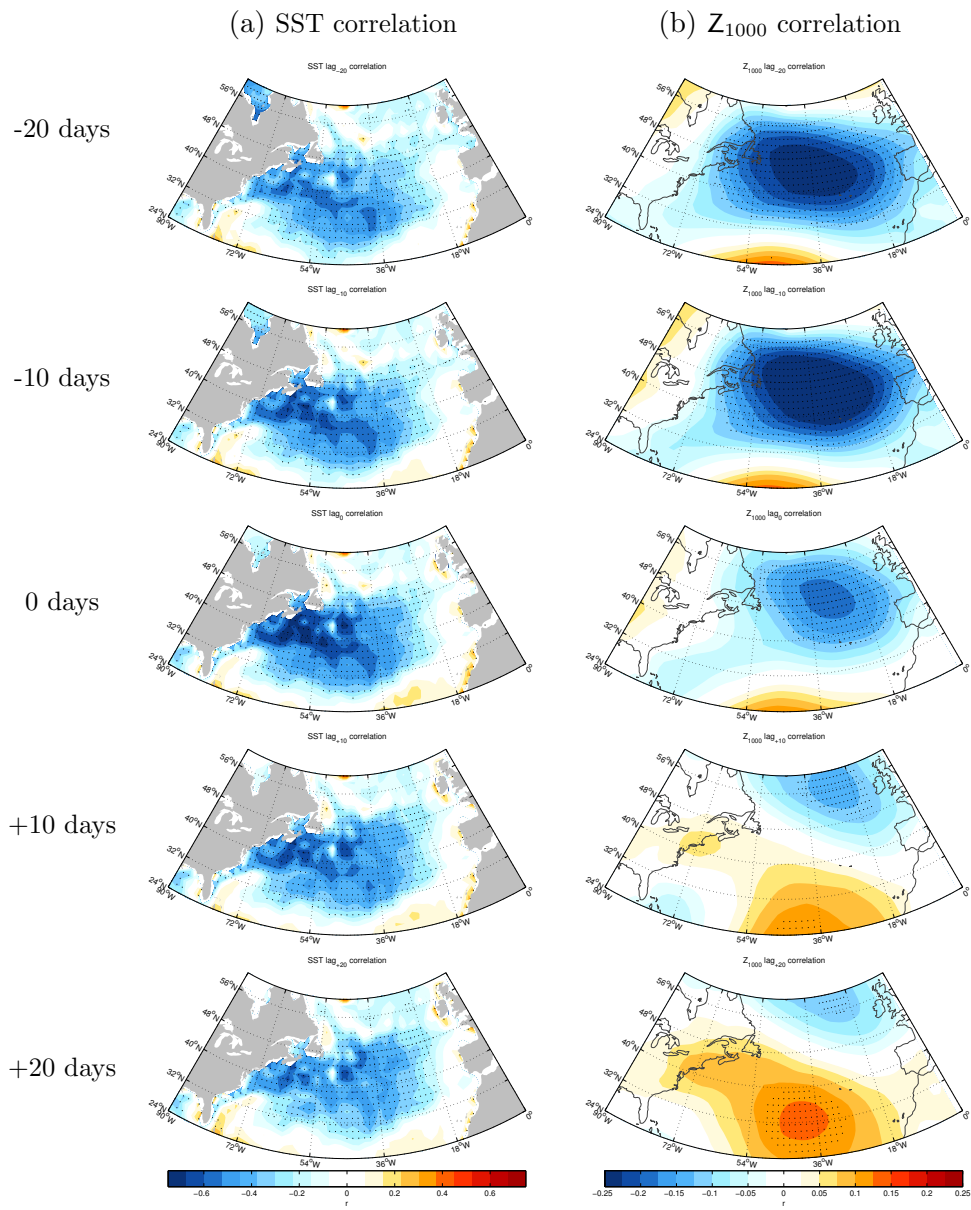


Figure 3.20 Correlations for a) SST and b) Z₁₀₀₀ on G_{SST} at all lags. Stippling indicates significance at the 2-tailed 95% confidence level.

correlations around the Gulf Stream region, as seen in Figure 3.20. Similar to the North Pacific, the significant SST results are expected at all lags because the SST field has a large heat capacity. As for the Z_{1000} results, the strong low present at negative lags is clearly significant at the 95% confidence level, indicating a robust atmospheric signature. At positive lags, the centers of the surface high and low are significant, with a clearly significant high present at +20-days. Hence, the North Atlantic residual signature in the Z_{1000} field at positive lag is similar to that found over the North Pacific (Figure 3.8), but is clearly more significant.

To further assess the robustness of the residual North Atlantic patterns, the SST and Z_{1000} lag regressions on G_{SST} were extended over the Northern Hemisphere to provide a hemispheric-scale perspective of the results. Figure 3.21 is a reproduction of Figure 3.17, but shows the results extended over the Northern Hemisphere. The pattern of Z_{1000} anomalies that drives the cold SST anomalies over the Gulf Stream Extension region is coincident with a large scale pattern of geopotential height anomalies that is reminiscent of the NAM. The low pressure over the North Atlantic that “drives” the SST anomalies is accompanied by a low over the North Pacific and, to a lesser extent, over Siberia. The NAM-like anomalies clearly decay by a lag of +10-days (column b).

At positive lags, the results reveal that the high over the North Atlantic is part of a larger wave train that appears to propagate downstream. By construction, the residual surface circulation pattern at positive lags (column c) is independent of the -20-day pattern. As is the case over the North Atlantic (Figure 3.17), the Northern Hemisphere regressions indicate two distinct patterns: one that decays with lag and one that grows with lag.

The Student’s T-test was applied to the SST and Z_{1000} lag correlations with G_{SST} to assess the regions where the results are significant at the 95% confidence level. The correlations are displayed in Figure 3.22. Now, in addition to the significant SST anomalies in the North Atlantic, we see significant positive and negative SST correlations in the North Pacific. The SST signal over the Pacific is consistent with an ENSO-like pattern, and suggests

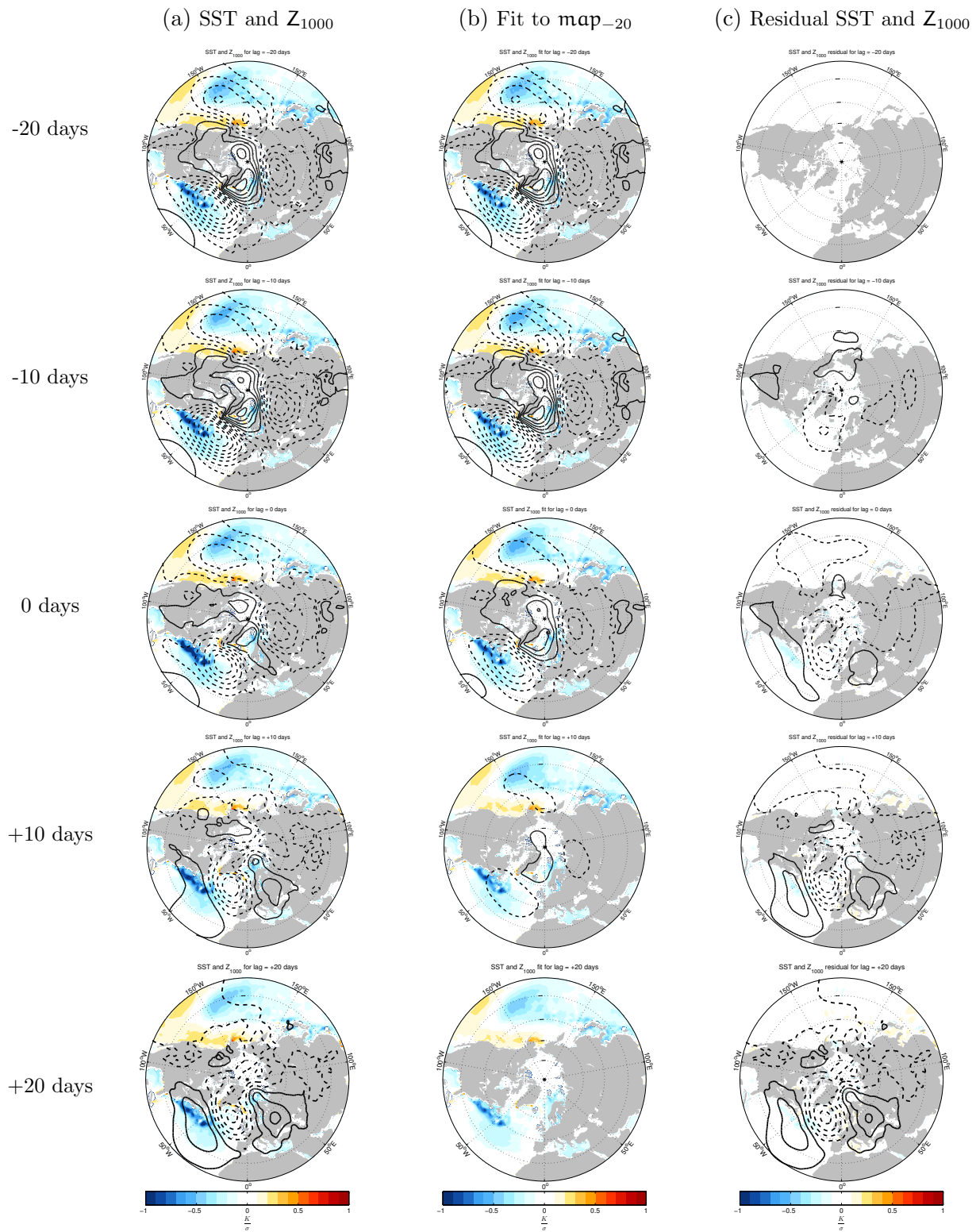


Figure 3.21 Same as in Figure 3.17, except for SST and Z_{1000} over the Northern Hemisphere.

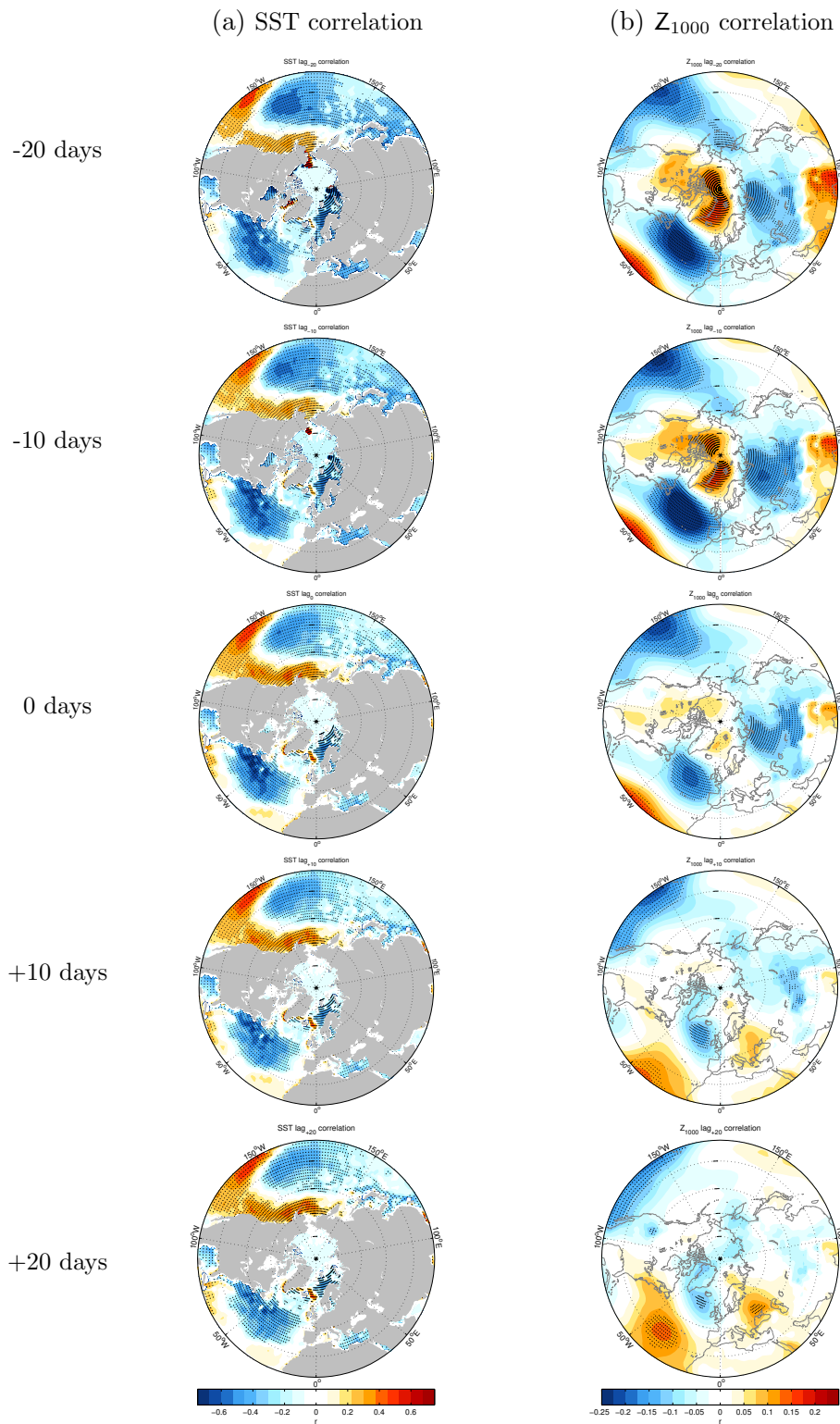


Figure 3.22 Correlations for a) SST and b) Z_{1000} on G_{SST} at all lags over the Northern Hemisphere. Stippling indicates significance at the 2-tailed 95% confidence level.

that the results are partially contaminated by ENSO variability. Since ENSO has little intraseasonal variability, ENSO is unlikely to account for the distinction between the results at negative and positive lag. As for the Z_{1000} correlations, there are many significant regions of highs and lows at the surface, especially at negative lags. At a lag of +20-days, the atmospheric wave emanating from the North Atlantic is the main significant feature over the Northern Hemisphere, aside from the region of significant negative correlations near the equatorial Eastern North Pacific (only the latter feature is evident at all lags).

3.2.2. NAM Index

As done for the Pacific sector, to test the reproducibility of the results based on the G_{SST} index, the analyses were repeated for an atmospheric (rather than an SST-based) index. Over the Pacific we used the PNA index; here we use the NAM index. In a previous study, Ciasto and Thompson [2004] investigated the relationship between SST anomalies and the NAM in the North Atlantic to determine if SST anomalies precede the atmospheric circulation. Here we extend their analysis using daily-mean data to observe relationships between SST anomalies and the NAM.

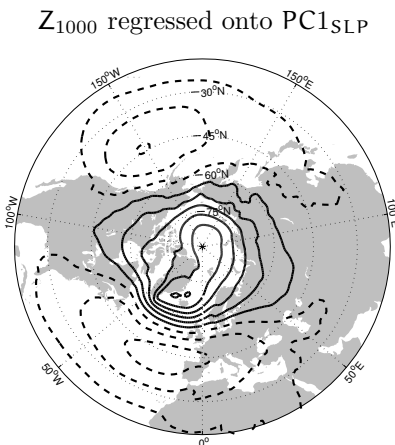


Figure 3.23 Contemporaneous monthly-mean Z_{1000} regressed on the NAM index, or the first principal component of SLP. The regression is indicative of the negative phase of the NAM. Solid (dashed) lines indicate positive (negative) contours with 10 meter interval spacing.

The NAM is the leading mode of wintertime atmospheric variability in the Northern Hemisphere, and the NAM index is obtained by calculating the first EOF of monthly-mean SLP [e.g., Wallace and Gutzler 1980; Quadrelli and Wallace 2004]. The daily time series of the NAM is obtained in a manner similar to that used to obtain the daily PNA index in the previous section. The characteristic Z_{1000} pattern associated with the NAM is illustrated in Figure 3.23. The negative phase of the NAM is associated with below-normal geopotential height anomalies over the central North Atlantic and the North Pacific with above-normal geopotential height anomalies over the Arctic. The negative geopotential height anomaly at the surface shown in Figure 3.23 is similar to the pattern seen in the contemporaneous monthly-mean G_{SST} regression (Figure 3.13). The similarities and differences between results derived for the oceanic and atmospheric indices for the North Atlantic will be investigated in this section.

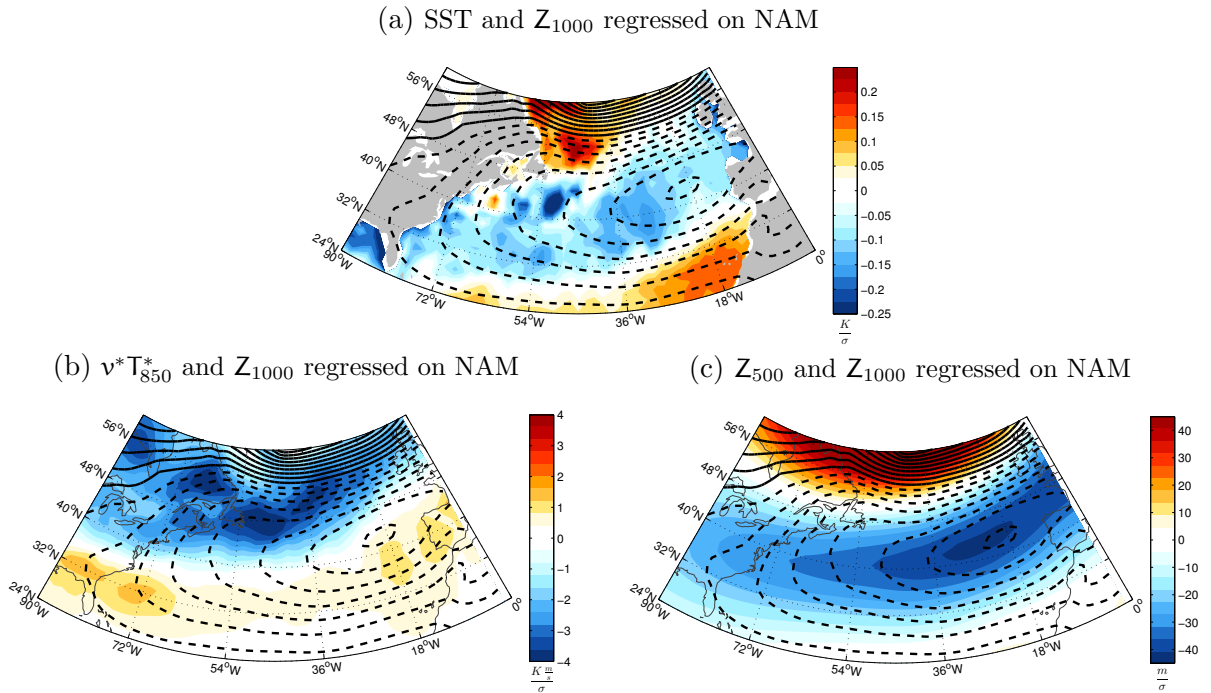


Figure 3.24. Contemporaneous DJF monthly regressions on the NAM for Z_{1000} (contours) and a) SST, b) $v^*T_{850}^*$, and c) Z_{500} (shading). Red (blue) shading indicates positive (negative) values, and solid (dashed) lines represent positive (negative) contours, with interval spacing of 4 meters between contours.

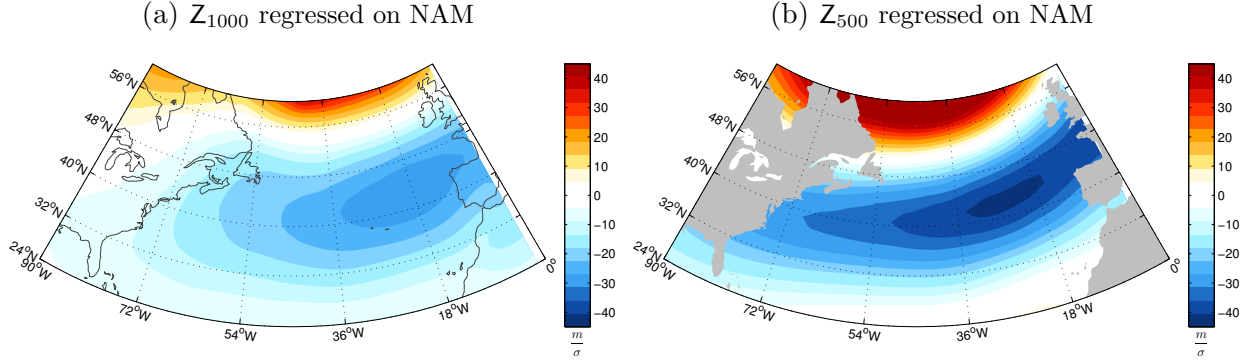


Figure 3.25. Same as in Figure 3.24, except for a) Z_{1000} and b) Z_{500} regressed on the NAM.

Figure 3.24 shows the monthly-mean contemporaneous regressions of SST, $\mathbf{v}^*T_{850}^*$, Z_{1000} , and Z_{500} on standardized values of the NAM index. Anomalous geopotential height falls are present in the central eastern North Atlantic with what appears to be the southern edge of a strong high pressure to the north. The SST field resembles a tripole pattern where 1) warm subpolar SSTs are associated with warm air advection (note the mean temperature gradient indicated in Figure 2.1) due to anomalously easterly flow along $\sim 55^\circ\text{N}$, 2) cold SSTs are associated with cold air advection due to anomalously northerly flow in the western part of the low, and 3) warm subtropical SSTs are associated with westerly flow along $\sim 25^\circ\text{N}$ that is advecting warmer air towards northwestern Africa. This result, the SST tripole, is known to follow the NAM and has been well documented in past studies [*e.g.*, Cayan 1992; Visbeck *et. al.* 2003; Ciasto and Thompson 2004]. As for the $\mathbf{v}^*T_{850}^*$ field, negative anomalies occur in the northern portion of the low with weak positive anomalies to the south. Figure 3.25 reveals that both the positive and negative geopotential height anomalies extend and strengthen with height. There are some general similarities in the regressions between G_{SST} and the NAM (compare Figures 3.13 and 3.24) such as negative SST anomalies around the Gulf Stream Extension and the low over the North Atlantic basin.

Lag regression analysis was performed on the NAM to further compare relationships with the atmospheric index to those associated with the ocean index. Figure 3.26.a confirms that the SST tripole pattern follows changes in the NAM index (as noted in Deser and Timlin

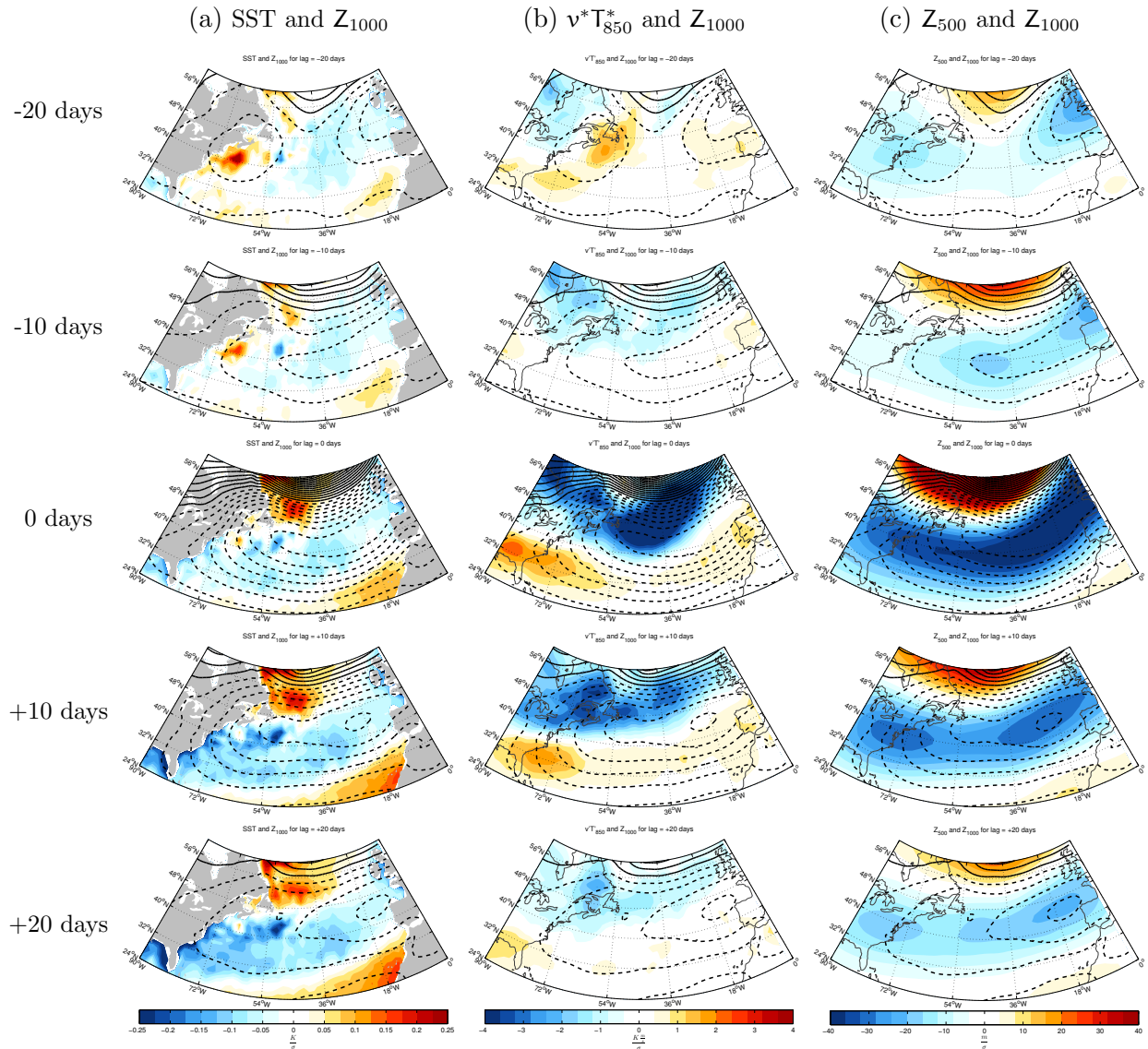


Figure 3.26 Lag regressions on the NAM for a) SST and Z_{1000} , b) $v^*T_{850}^*$ and Z_{1000} , and c) Z_{500} and Z_{1000} . Z_{1000} is shown in contours with solid (dashed) lines representing positive (negative) values at an interval spacing of 4 meters. Negative lags are indicative of the variables leading the NAM, and positive lags are indicative of the NAM leading the variables. Recall that the NAM index is fixed for the DJF time period.

[1997] and Ciasto and Thompsom [2004]). It is of interest to note that within the SST tripole, there is anomalously cold SST located within the region used to calculate the G_{SST} index. The strongest negative $v^*T_{850}^*$ anomalies occur at a lag of 0-days. The Z_{1000} and Z_{500} patterns in Figure 3.26.c are strongest at lag-0 (*i.e.*, they are coincident with the NAM) and decay through positive lags. The results indicate similarities between the anomalously low geopotential height related to the NAM and the geopotential height that precedes the G_{SST} index (Figure 3.15). Note that, while the SST tripole pattern does not clearly appear in the G_{SST} regressions, the locations of the negative SST anomalies for both indices are similar.

The results for the NAM confirm that the atmosphere influences SST anomalies in the North Atlantic [*e.g.*, Kushnir *et. al.* and authors therein]. As mentioned above, it is evident that a SST tripole pattern is responding to the NAM index. Within this pattern, a region of cold SST anomalies near the Gulf Stream Extension appears similar to those seen in the G_{SST} regressions. This result suggests that the NAM may be responsible for atmospheric circulation anomalies preceding the G_{SST} index. However, signatures in SST anomalies preceding the NAM appear less robust, and it remains less certain if significant SST anomalies precede the atmospheric index.

3.2.3. G_{SLP} Index

We also tested results based on an atmospheric index motivated by the wave train at positive lags in the G_{SST} regressions. The new atmospheric index, hereafter referred to as G_{SLP} , represents the anomalous Z_{1000} +20-day lag pattern in Figure 3.21 and was calculated as follows: 1) Z_{1000} time series were calculated at three locations: A) the center of the high in the North Atlantic (48°W, 36°N), B) the center of the low over Iceland (24°W, 60°N), and C) the center of the high over Europe (42°E, 51°N). 2) The G_{SLP} time series was defined as $A - B + C$, and 3) the resulting index was standardized so that positive values of the index are associated with positive Z_{1000} anomalies over the Gulf Stream region.

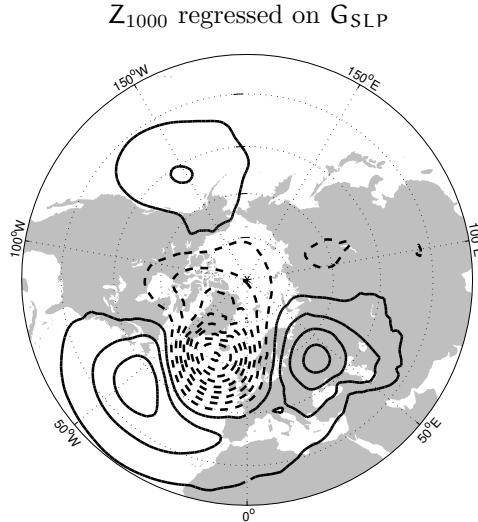


Figure 3.27 Contemporaneous Z_{1000} regressed on the G_{SLP} index. Solid (dashed) lines indicate positive (negative) contours with 10 meter interval spacing.

The regressions of Z_{1000} onto G_{SLP} can be seen in Figure 3.27. By construction, the index captures the wave emanating from the North Atlantic, as shown in Figure 3.21.a. However, it also captures a weak high over the Eastern North Pacific that is not apparent in the +20-day pattern in Figure 3.21. The link between the North Pacific and North Atlantic in Figure 3.27 suggests that the G_{SLP} index samples the PNA pattern [*e.g.*, Wallace and Thompson 2002].

The autocorrelations of the NAM, PNA, and G_{SLP} indices are shown in Figure 3.28. As noted in previous work [*e.g.*, Feldstein 2000], the NAM index has an e-folding timescale of approximately 10 days and the PNA index has an e-folding timescale of approximately 8 days. In the analysis, the NAM and PNA indices also yield e-folding timescales on the order of a week. The autocorrelation indicates that the G_{SLP} index has an e-folding timescale of approximately 5 days. As the G_{SLP} index occurs at the shortest timescale, it is less red compared to the NAM and the PNA. Despite the differing e-folding timescales, it is unclear if the autocorrelation of the G_{SLP} index is clearly distinguishable from the autocorrelations of the two leading modes of wintertime Northern Hemisphere atmospheric variability.

Autocorrelations of the NAM, PNA, and G_{SLP} Indices

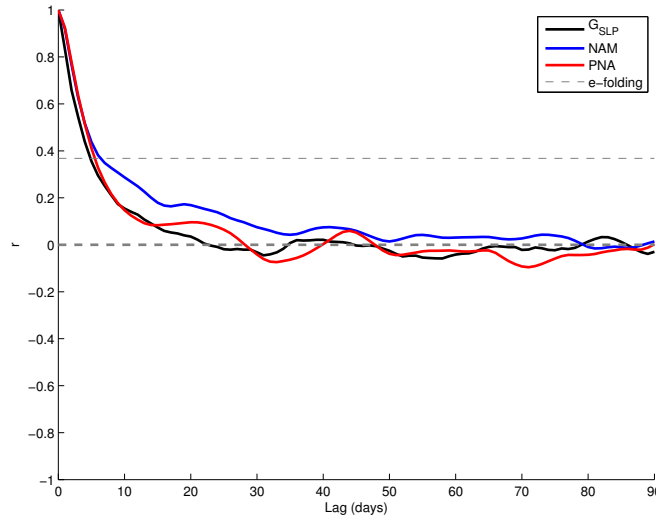


Figure 3.28 Autocorrelation of G_{SLP} (black), NAM (blue), and PNA (red).

Figure 3.29 shows the lag correlations between the G_{SST} , G_{SLP} , and NAM indices. As depicted in Figure 3.29.a, the correlations between G_{SST} and the NAM exceed the 95% confidence level at negative lags, indicating that the NAM significantly leads the SST anomalies over the Gulf Stream region. Correlations between G_{SST} and the NAM at positive lags are only weakly significant. This result is expected as the NAM is known to lead the North Atlantic SST tripole pattern [e.g., Cayan 1992; Visbeck *et. al.* 2003; Ciasto and Thompson 2004]. Recall that the SST regressions onto the G_{SST} and NAM indices (Figures 3.13.a and 3.24.a, respectively) indicated similar negative SST anomalies in the vicinity of the Gulf Stream Extension. The G_{SST} and NAM lag correlations provide additional evidence that SST anomalies associated with the G_{SST} index are likely a component of the SST tripole, which is forced by the NAM.

As evidenced in Figure 3.29.b, lag correlations between the G_{SST} and G_{SLP} indices are significant at positive and negative lags. While this result indicates that SST anomalies in the vicinity of the Gulf Stream precede the G_{SLP} index, we see that the atmospheric index also precedes the G_{SST} index with roughly the same amplitude. If the SST anomalies were exclusively responsible for forcing the wave train pattern, we would expect the negative lag

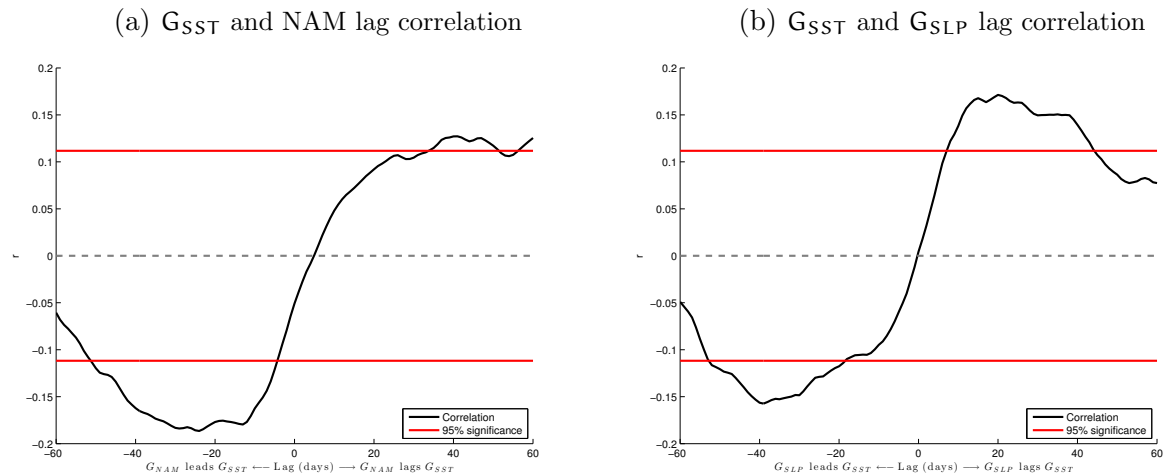


Figure 3.29. Lag correlations of a) G_{SST} and the NAM and b) G_{SST} and G_{SLP} . Red lines indicate correlations that exceed the 95% confidence level.

correlations to be near zero and then spike towards positive lag [*e.g.*, Barsugli and Battisti 1998; Lorenz and Hartmann 2001]. Thus, the analysis using the G_{SLP} index does not provide clear evidence of SST anomalies in the vicinity of the Gulf Stream forcing the overlying atmosphere.

CHAPTER 4: DISCUSSION AND CONCLUSIONS

We have investigated the observed relationships between midlatitude SST anomalies and the atmospheric circulation in the Northern Hemisphere. The primary tool we have used is lag regressions based on daily-resolution observations of SST and SLP over the North Pacific and North Atlantic Oceans. In this chapter, we discuss the results in the context of previous studies, summarize the key findings, and outline areas of future research.

4.1. Discussion

Consistent with previous studies [*e.g.*, Deser and Timlin 1997; Kushnir *et. al.* 2002 and authors therein; Ciasto and Thomson 2004], lag regressions onto the indices of SSTs and atmospheric circulation over the North Pacific and Atlantic regions indicate that atmospheric variability strongly forces SST anomalies, *i.e.*, the atmosphere leads variations in the SST field by approximately 2-3 weeks. Regressions onto the K_{SST} and G_{SST} indices (SSTs averaged over the Kuroshio-Oyashio and Gulf Stream Extension regions, respectively) show that cold SST anomalies in the vicinity of the WBCs are preceded by strong surface lows in each basin, consistent with northerly (cold) advection over the SST anomalies (Figures 3.1 and 3.13). The negative geopotential height anomalies are largest at negative lags, suggesting that cold air advection on the western side of the low is responsible for setting up the SST anomalies (Figures 3.3 and 3.15). Similarly, the “SST tripole” pattern is seen lagging variability in the NAM (Figure 3.26), further confirming the ocean’s response to the anomalous atmospheric circulation in the North Atlantic [*e.g.*, Cayan 1992; Visbeck *et. al.*, 2003; Ciasto and Thompson 2004].

However, the observational analysis also reveals distinct patterns of atmospheric circulation anomalies that lag changes in the SST field in each ocean basin. The patterns of atmospheric circulation anomalies that lag the SST field are distinctly different from those

that precede it. The lagged “response” of the atmosphere is most pronounced over the Atlantic. Here, large positive geopotential height anomalies form above cold SST anomalies over the Gulf Stream region at a lag of several weeks. The formation of the surface high is consistent with the hydrostatic response to cold thermal forcing. Relatively cold SSTs lead to the compression of isentropes in the overlying column of air, creating a pressure difference aloft between the region of cold SST anomalies and the surrounding areas. Since air flows from high to low pressure, the pressure gradients aloft give rise to a thermally direct circulation, with sinking motion above the surface high. The result is broadly consistent with Minobe *et. al.* [2008, 2010], who invoked the pressure adjustment mechanism for explaining the pattern of long-term mean atmospheric convection in the vicinity of the Gulf Stream. Recall that the pressure adjustment mechanism suggests that SSTs modify the MABL air temperature and thus induce pressure perturbations near the surface. A notable caveat to our results is that the lag regressions may simply indicate the evolution of atmospheric circulation anomalies that occurs independently of the cold SSTs. Nevertheless, it is clear that anomalous atmospheric circulation patterns that lag the SST anomalies have distinctly different structures than those that precede the SST anomalies.

The results based on the eddy heat fluxes are less clear. As noted in Chapter 1, Sampe *et. al.* [2010] proposed a mechanism for the influence of an ocean front on the overlying atmosphere (Figure 1.6). The sharp SST contrast across the front induces changes in near-surface baroclinicity, which in turn leads to enhanced poleward eddy heat fluxes. However, unlike Sampe *et. al.* [2010] who focused on the long-term mean (which includes larger SST gradients), our analysis focuses on regions of SST anomalies (which are associated with relatively small gradients in SSTs) in the vicinity of ocean fronts rather than the influence of the front itself. In the North Pacific, Figure 3.6 reveals that the $\mathbf{v}^*T_{850}^*$ anomalies at lag-0 are mostly related to atmospheric forcing along $\sim 35^\circ\text{N}$ in the vicinity of surface westerlies and thus the atmospheric storm track. By positive lag, while there is a slight indication of positive $\mathbf{v}^*T_{850}^*$ anomalies on the northwestern side of the surface high,

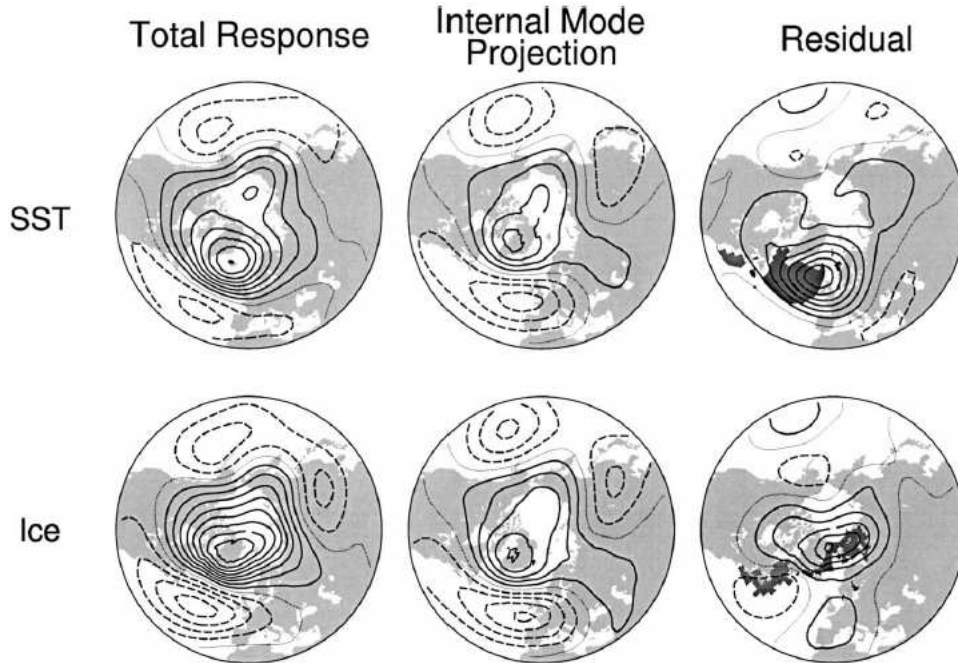


Figure 4.1. Courtesy of Deser *et. al.* [2004]. Decomposition of the (left) total wintertime Z_{500} response to (top) SST and (bottom) sea ice into the (middle) indirect response and (right) direct response. Solid (dashed) lines indicate positive (negative) contours, spaced at 10m. Shading in the residual panels indicates the locations of the SST and sea ice anomalies.

the results are not significant. In the North Atlantic, although the $v^*T_{850}^*$ anomalies appear more robust by the +20-day lag (Figure 3.18), it remains unclear if the eddy heat fluxes are responding directly to the SST anomalies or to the anomalous circulation.

We also examined the component of the regressions that are linearly congruent with and independent of the “atmospheric forcing” at negative lags. In their numerical study, Deser *et. al.* [2004] decomposed the simulated geopotential height response to observed SST patterns into two parts: 1) a component that projects onto the leading mode of atmospheric variability (the “indirect response”) and 2) a component that represents the residual portion (the “direct response”). The results indicated that the indirect response dominates the total simulated geopotential height pattern in the North Atlantic and resembles the NAM (Figure 4.1). The analogous spatial linear decompositions in our observational analyses yield similar results to their numerical study. Figures 3.5 and 3.17 indicate that the “atmospheric forcing” component dominates the Z_{1000} patterns in the lag-0 regressions in each basin.

However, towards positive lag (when the atmosphere lags the ocean) the component related to the “atmospheric forcing” becomes damped, and the residual pattern (“the atmospheric response”) is very similar to the total regression. Thus, the patterns at positive lag are, by construction, independent of the patterns of “atmospheric forcing” at negative lags. Unlike Deser *et. al.* [2004], who found the direct response to be baroclinic in nature, our residual geopotential height patterns are largely barotropic; positive Z_{1000} anomalies coincide with positive Z_{500} anomalies that are shifted slightly southwestward with height. Our analysis confirms the utility of decomposing the regressions into a portion related to the atmospheric forcing and a portion that is independent of the atmospheric forcing.

4.1.1. North Pacific Circulation Results

The anomalous high geopotential heights at positive lag in regressions based on SSTs averaged over the Kuroshio-Oyashio Extension region are similar to findings reported in Frankignoul *et. al.* [2011]. In their observational study, north-south shifts in the Kuroshio and Oyashio Extension fronts precede equivalent barotropic anomalies reminiscent of the North Pacific Oscillation (NPO) [*e.g.*, Walker and Bliss 1932; Linkin and Nigam 2008]. The NPO is characterized by a north-south seesaw in SLP in the North Pacific. In addition to the NPO pattern, Frankignoul *et. al.* [2011] found an equivalent barotropic high in the northwestern North Pacific in association with a northward shift of the Kuroshio Extension (*i.e.*, warm SST anomalies over the Kuroshio Extension). Our analysis yields a similar north-south seesaw in geopotential height associated with cold SST anomalies in the North Pacific Ocean (Figure 3.3), with a surface high near the Kuroshio-Oyashio Extension and a surface low centered over Alaska.

Although positive lags yield an NPO-like circulation pattern, the geopotential height anomalies are not significant assuming 1 degree of freedom per 10 days at the 95% confidence level (Figure 3.8). It should be noted that we used conservative degrees of freedom for the

Student’s T-test. Using the method to calculate an effective sample size (N_{eff}) as described in Santer *et. al.* 2000 yields a larger number of degrees of freedom for the geopotential height field. When we repeat the significance test using N_{eff} (not shown), the NPO-like circulation anomalies are significant. Hence, we view the SLP “response” over the North Pacific sector as being on the fringe of significance. Likewise, our analyses based on the PNA index do not reveal a pattern of significant SST anomalies preceding variations in the atmospheric circulation (Figure 3.12). Rather, the results based on the PNA are dominated by a region of cold SST anomalies in the eastern North Pacific that lag the surface low associated with the PNA.

4.1.2. North Atlantic Circulation Results

Unlike the “response” in the atmospheric circulation to variations in the Kuroshio-Oyashio Extension, the “response” to variations in the Gulf Stream Extension are seemingly robust. In particular, the high geopotential height anomalies that lie downwind of the Gulf Stream at positive lag are significant at the 95% confidence level (Figure 3.20). As for regressions on the NAM index, despite a small region of warm SST anomalies near the North American coastline that precede the NAM (Figure 3.26), the analysis suggests that the largest SST anomalies lag rather than lead the atmospheric circulation. Hence, the lag regressions against the NAM index do not support SST forcing of the annular mode, but the significant geopotential height anomalies lagging the G_{SST} index provide evidence of a unique “atmospheric response” to SST anomalies in the Gulf Stream region.

Extending the analysis to the Northern Hemisphere, we found that the surface high that lies downwind of the Gulf Stream at positive lags is part of a larger wave train in the geopotential height field, with out of phase centers of action extending over the northern Eurasian sector. The spatial linear decomposition confirms that the wave train at positive lags is linearly independent of the NAM-like anomalies that appear at negative lags. As

previously mentioned, the independence of the pattern at positive lags from the pattern at negative lags does not prove that the atmospheric circulation is responding to negative SST anomalies in the vicinity of the Gulf Stream. But it is tempting to conclude that is it. As discussed later in this section, testing the atmospheric response to anomalies in the Gulf Stream Extension in numerical simulations will form the basis for my future work.

We also constructed a G_{SLP} index (based on the wave train at positive lag) to determine if anomalously cold SSTs robustly precede variations in the amplitude of the wave train. The results are inconclusive. However, as shown in Figure 3.27, the Z_{1000} regression onto the G_{SLP} index indicates that it does not uniquely isolate the wave train at positive lags, but is biased by positive geopotential height anomalies in the North Pacific, which suggests that a component of the PNA is being captured in our G_{SLP} index [*e.g.*, as per the Atlantic signal of the PNA; Wallace and Thompson 2002]. As such, the lag correlations between the G_{SST} and G_{SLP} indices (Figure 3.29.b) do not reveal a clear pattern of lag correlations as might be expected if the ocean was forcing the G_{SLP} index.

4.2. Conclusions

Daily-resolution observations have been analyzed to investigate ocean-atmosphere interactions on transient timescales during the winter season near WBCs in the Northern Hemisphere midlatitude oceans. We have used SST indices motivated by regions of high SST variability in the vicinity of the Kuroshio-Oyashio Extension (K_{SST}) in the North Pacific and the Gulf Stream Extension (G_{SST}) in the North Atlantic to examine the lead/lag relationships between SST and atmospheric variables such as the eddy heat flux and geopotential height. The observational analysis provides new context for understanding the time varying structure of the patterns of atmospheric variability associated with variations in SSTs over the western boundary currents.

Over each basin, the lag regressions suggest that SST anomalies respond to anomalous atmospheric circulation patterns, consistent with results from previous studies which have established that the midlatitude atmosphere forces the underlying ocean. In our analysis, negative SST anomalies in the vicinity of the WBCs are formed by cold air advection from northerly flow on the western side of a surface low that sits over the center of the ocean basin. Regressions based on indices of the leading modes of atmospheric variability in the Northern Hemisphere also suggest that anomalous SSTs tend to follow, not lead, atmospheric variability. Lag regressions for both the SST and atmospheric indices indicate that geopotential height anomalies peak approximately 2-3 weeks before the onset of the SST anomalies, consistent with results by Deser and Timlin [1997] and Ciasto and Thompson [2004].

However, our results have also uncovered a robust, albeit weaker, pattern of atmospheric anomalies that lag the SST field. As the pattern of atmospheric forcing decays from negative lag to positive lag, a new pattern with positive geopotential height anomalies located over negative SST anomalies forms at lags of ~ 10 -20 days following peak amplitude in the SST field. The surface high that lags the G_{SST} index in the North Atlantic is more pronounced than that associated with the K_{SST} index in the North Pacific (where the results are found to be on the fringe of significance). In the North Atlantic, the robust surface high appears to be part of an atmospheric wave train extending downstream, with a low over Iceland and a high over northern Europe. In each basin, the anomalous atmospheric circulation at positive lags is clearly distinct from that found at negative lags.

The central results are made clear by the novel approach of applying spatial linear decomposition to the regression analysis. Motivated by the distinct difference between the +20-day lag and -20-day lag patterns, we decomposed the regression patterns into two distinct components: one that is linearly congruent with the -20-day lag pattern (the “atmospheric forcing”) and one that is independent of it. The results were interpreted as follows:

For regressions onto the K_{SST} and G_{SST} indices, the atmospheric regressions can be interpreted as the superposition of two patterns:

- a pattern that peaks approximately 2-3 weeks before the SST anomalies (the “atmospheric forcing” or “fit”) and decays through lag-0
- a pattern that peaks approximately 2-3 weeks after the SST anomalies (the “atmospheric response” or “residual”).

In a sense, the technique allows us to separate out patterns related to atmospheric forcing and patterns potentially related to ocean forcing. Over both basins, we found the positive geopotential height anomalies at positive lag to be mostly independent from the patterns of atmospheric forcing. The decompositions also confirmed that the wave train pattern that lags the G_{SST} index is independent of the pattern of atmospheric forcing.

We emphasize that observational analyses alone can not “prove” that the SST field is forcing the pattern of atmospheric circulation anomalies that lag the K_{SST} and G_{SST} indices. Though the residual patterns in the decomposition analysis are, by construction, independent from the “atmospheric forcing” patterns, the technique does not prove forcing by the ocean. It is possible that the residual circulation patterns that lag the SST anomalies could be responding to an independent form of climate variability, or may indicate the time evolution of the atmosphere independent of the SST field. The lag correlations between the G_{SST} and G_{SLP} indices do not indicate that one system is clearly forcing the other.

Hence, we are unable to conclude from the observations that midlatitude SST anomalies in the vicinity of the Kuroshio-Oyashio and Gulf Stream WBCs influence the overlying atmospheric circulation. But we are able to conclude that midlatitude SST anomalies lead a robust pattern of atmospheric circulation anomalies that is consistent with the theoretical response of the midlatitude atmosphere to SST anomalies (*i.e.*, cold SSTs balanced by high pressure downstream). Below I discuss ideas for future work that follows from the current study.

4.3. Future Work

This thesis raises a series of questions regarding the influence of the midlatitude SST field on the atmospheric flow. Below I propose areas of future research to further explore midlatitude ocean-atmosphere interaction motivated by the observational analyses presented here.

4.3.1. Linearity of the Response

The results of this thesis focus on atmospheric circulation anomalies associated with below-average rather than above-average SSTs in the midlatitude oceans. Deser *et. al.* [2004] noted that the response to a warm SST anomaly is opposite *but unequal* in magnitude compared to that for a cold SST anomaly. In their study, the authors reason that this inequality is due to the stabilizing effect of surface cooling in comparison to the destabilizing effect of surface warming. The destabilizing effect of warm SST anomalies is hypothesized to result from vertical turbulent mixing where surface warming (increased SST) reduces the static stability in the overlying column of air, leading to mixing that brings faster winds to the surface [*e.g.*, O'Neill *et. al.* 2003; Nonaka and Xie 2003].

With the nonlinearity of the atmosphere's response to anomalous surface heating in mind, I would like to extend the analysis presented in this thesis to observations with warm SST anomalies in the vicinity of the WBCs. To do this, we would use composite analysis, which makes no assumption about linearity. This technique consists of sorting data into categories and comparing the means of each category. In this case, we would compare the mean SLP associated with ± 1 standard deviation or greater of SST. This will provide a quantitative measure of the linearity of the atmosphere's response to positive and negative surface heating. As surface highs were collocated with persistent negative SST anomalies at positive lag, we would expect surface (thermal) lows to be coincident with positive SST

anomalies at positive lag. However, it will be interesting to see if the composite analysis supports 1) stronger circulation (horizontal and vertical) anomalies associated with positive surface heating in each ocean basin and 2) an opposite (yet unequal?) wave train pattern in the North Atlantic.

4.3.2. AMSR-E Observational Analysis

As mentioned in the data and methods chapter, the observational analyses in this thesis were performed using the ERA-Interim reanalysis product at a spatial resolution of 1.5° across the globe. Future work would benefit from assessing the reproducibility of the results by repeating the analyses with higher spatial resolution observations, such as those provided by the Advanced Microwave Scanning Radiometer-EOS (AMSR-E) dataset. In this dataset, observations were collected at a spatial resolution of 0.25° sampled twice-daily across the globe. However, the caveat to this dataset is the temporal coverage as the satellite was operational only between June 1, 2002 through October 4, 2011, allowing for only 8 observed winter seasons (compared to 32 winter seasons for ERA-Interim).

Despite the decreased temporal coverage, AMSR-E would provide higher spatial resolution data for the observational analyses to be compared against analyses using the lower resolution ERA-Interim output. A numerical study by Smirnov *et. al.* [2014b] has suggested the importance of model resolution for resolving midlatitude air-sea interaction. They found that the high-resolution GCM responded with deeper vertical motion to a meridional shift of the Kuroshio-Oyashio SST front in the North Pacific compared to the low-resolution GCM. While higher resolution data would not likely alter the observed large-scale atmospheric patterns associated with the K_{SST} and G_{SST} indices, we believe that AMSR-E data would provide insight into relationships on smaller scales that are less resolved in the lower resolution output from ERA-Interim, such as the boundary layer response to finer patterns of anomalous SSTs and local responses (*i.e.*, vertical motion) in the free atmosphere.

4.3.3. Numerical SST Experiments

The analyses in this thesis focus on observational data to investigate midlatitude ocean-atmosphere relationships on transient timescales. Future work would benefit from performing numerical studies based on this research. We could reapply our analyses to data from existing coupled GCM runs, such as those provided by the National Centers for Atmospheric Research Community Earth System Model (NCAR CESM), and compare the results to those presented in this thesis. It would be interesting to see if the “atmospheric forcing” and the “atmospheric response” patterns hold for output from long coupled simulations.

Furthermore, we could use an AGCM to run simulations with forced SST anomalies, analogous to the experiments performed in Smirnov *et. al.* [2014b]. The model used in their study, the NCAR Community Atmosphere Model version 5 (CAM5), is a newer atmospheric global climate model with a fixed ocean. Given the fixed ocean in CAM5, we could impose SST anomalies in the vicinity of the Kuroshio-Oyashio and Gulf Stream Extension regions similar to those observed in the thesis. It would be interesting to see if the atmospheric model responds to the SST anomalies with pressure perturbations comparable to those observed lagging the K_{SST} and G_{SST} indices. Specifically, we are curious to see if we can obtain an atmospheric wave train response to negative SST anomalies in the vicinity of the Gulf Stream as suggested by the observational analyses. The forced SST experiments would be used to increase our understanding of the results presented in the thesis as well as the implications for midlatitude ocean forcing of the atmosphere.

REFERENCES

- Alexander, M.A., C. Deser, M.S. Timlin, 1997: The Reemergence of SST Anomalies in the North Pacific Ocean. *J. Climate*, **12**, 2419 - 2433.
- Barsugli, J.J., and D.S. Battisti, 1998: The Basic Effects of Atmosphere-Ocean Thermal Coupling on Midlatitude Variability. *J. Atmos. Sci.*, **55**, 477 - 493.
- Battisti, D.S., U.S. Bhatt, and M.A. Alexander, 1995: A Modeling Study of the Interannual Variability in the Wintertime North Atlantic Ocean. *J. Climate*, **8**, 3067 - 3083.
- Cayan, D.R., 1992: Latent and Sensible Heat Flux Anomalies over the Northern Oceans: Driving the Sea Surface Temperature. *J. Phys. Oceanogr.*, **22**, 859 - 881.
- Chelton, D.B., S.K. Esbensen, M.G. Schlax, N. Thum, M.H. Freilich, F.J. Wentz, C.L. Gentemann, M.J. McPhaden, and P.S. Schopf, 2001: Observations of Coupling between Surface Wind Stress and Sea Surface Temperature in the Eastern Tropical Pacific. *J. Climate*, **14**, 1479 - 1498.
- Chelton, D.B., M.G. Schlax, M.H. Freilich, and R.F. Milliff, 2004: Satellite Measurements Reveal Persistent Small-Scale Features in Ocean Winds. *Science*, **303**, 978 - 983.
- Chelton, D.B., and S.-P. Xie, 2010: Coupled ocean-atmosphere interaction at oceanic mesoscales. *Oceanography*, **23**, 52 - 69.
- Ciasto, L.M., and D.W.J. Thompson, 2004: 2004: North Atlantic Atmosphere-Ocean Interaction on Intraseasonal Time Scales. *J. Climate*, **17**, 1617 - 1621.
- Czaja, A., and C. Frankignoul, 2002: Observed Impact of Atlantic SST Anomalies on the North Atlantic Oscillation. *J. Climate*, **15**, 606 - 623.
- Davis, R.E., 1976: Predictability of Sea Surface Temperature and Sea Level Pressure Anomalies over the North Pacific Ocean. *J. Phys. Oceanogr.*, **6**, 249 - 266.

- Davis, R.E., 1978: Predictability of Sea Level Pressure Anomalies Over the North Pacific Ocean. *J. Phys. Oceanogr.*, **8**, 233 - 246.
- Deser, C., and M.S. Timlin, 1997: Atmosphere-Ocean Interaction on Weekly Timescales in the North Atlantic and Pacific. *J. Climate*, **10**, 393 - 408.
- Deser, C., G. Magnúsdóttir, R. Saravanan, and A. Phillips, 2004: The Effects of North Atlantic SST and Sea Ice Anomalies on the Winter Circulation in CCM3. Part II: Direct and Indirect Components of the Response. *J. Climate*, **17**, 877 - 889.
- Diaz, H.F., M.P. Hoerling, and J.K. Eischeid, 2001: ENSO Variability, Teleconnections and Climate Change. *Int. J. Climatol.*, **21**, 1845 - 1862.
- Feldstein, S.B., 2000: The Timescale, Power Spectra, and Climate Noise Properties of Teleconnection Patterns. *J. Climate*, **13**, 4430 - 4440.
- Frankignoul, C., and K. Hasselmann, 1977: Stochastic climate models. Part II: Application to sea-surface temperature anomalies and thermocline variability. *Tellus*, **29**, 284 - 305.
- Frankignoul, C., and R.W. Reynolds, 1983: Testing a Dynamical Model for Mid-Latitude Sea Surface Temperature Anomalies. *J. Phys. Oceanogr.*, **13**, 1131 - 1145.
- Frankignoul, C., 1985: Sea Surface Temperature Anomalies, Planetary Waves, and Air-Sea Feedback in the Middle Latitudes. *Rev. Geophys.*, **23**, 357 - 390.
- Frankignoul, C., N. Sennechal, Y-O. Kwon, and M.A. Alexander, 2011: Influence of the Meridional Shifts of the Kuroshio and the Oyashio Extensions on the Atmospheric Circulation. *J. Climate*, **24**, 762 - 777.
- Graham, N.E., T.P. Barnett, R. Wilde, M. Ponater, and S. Schubert, 1994: On the Roles of Tropical and Midlatitude SSTs in Forcing Interannual to Interdecadal Variability in the Winter Northern Hemisphere Circulation. *J. Climate*, **7**, 1416 - 1441.

- Haney, R.L., 1985: Midlatitude Sea Surface Temperature Anomalies: A Numerical Hind-cast. *J. Phys. Oceanogr.*, **15**, 787 - 799.
- Hoskins, B.J., and D.J. Karoly, 1981: The Steady Linear Response of a Spherical Atmosphere to Thermal and Orographic Forcing. *J. Atmos. Sci.*, **38**, 1179 - 1196.
- Hayes, S.P., J. McPhaden, J.M. Wallace, 1989: The Influence of Sea-Surface Temperature on Surface Wind in the Eastern Equatorial Pacific: Weekly to Monthly Variability. *J. Climate*, **2**, 1500 - 1506.
- Kushnir, Y., and I.M. Held, 1996: Equilibrium Atmospheric Response to North Atlantic SST Anomalies. *J. Climate*, **9**, 1208 - 1220.
- Kushnir, Y., W.A. Robinson, I. Blade, N.M.J. Hall, S. Peng, and R. Sutton, 2002: Atmospheric GCM Response to Extratropical SST anomalies: Synthesis and Evaluation. *J. Climate*, **15**, 2233 - 2256.
- Kwon, Y.-O., and T. M. Joyce, 2013: Northern Hemisphere Winter Atmospheric Transient Eddy Heat Fluxes and the Gulf Stream and Kuroshio-Oyashio Extension Variability. *J. Climate*, **26**, 9839 - 9859.
- Lau, N.-C., and M.J. Nath, 1994: A Modeling Study of the Relative Roles of Tropical and Extratropical SST Anomalies in the Variability of the Global Atmosphere-Ocean System. *J. Climate*, **7**, 1184 - 1207.
- Linkin, M.E., and S. Nigam, 2008: The North Pacific Oscillation-West Pacific Teleconnection Pattern: Mature-Phase Structure and Winter Impacts. *J. Climate*, **21**, 1979 - 1997.
- Lorenz, D.J., and D.L. Hartmann, 2001: Eddy-Zonal Flow Feedback in the Southern Hemisphere. *J. Atmos. Sci.*, **58**, 3312 - 3327.

- Minobe, S., A. Kuwano-Yoshida, N. Komori, S-P. Xie, and R.J. Small, 2008: Influence of the Gulf Stream on the troposphere. *Nature*, **452**, 206 - 210.
- Minobe, S., M. Miyashita, A. Kuwano-Yoshida, H. Tokinaga, and S-P. Xie, 2010: Atmospheric Response to the Gulf Stream: Seasonal Variations. *J. Climate*, **23**, 3699 - 3719.
- Nakamura, H., G. Lin, and T. Yamagata, 1997: Decadal Climate Variability in the North Pacific during the Recent Decades. *Bull. Amer. Meteor. Soc.*, **78**, 2215 - 2225.
- Nakamura, H., T. Sampe, A. Goto, W. Ohfuchi, and S-P. Xie, 2008: On the importance of midlatitude oceanic frontal zones for the mean state and dominant variability in the tropospheric circulation. *Geophys. Res. Lett.*, **35**, L15709, doi:10.1029/2008GL034010.
- Nonaka, M., and S-P. Xie, 2003: Covariations of Sea Surface Temperature and Wind over the Kuroshio and Its Extension: Evidence for Ocean-to-Atmosphere Feedback, *J. Climate*, **16**, 1404 - 1413.
- O'Neill, L.W., D.B. Chelton, and S.K. Esbensen, 2003: Observations of SST-Induced Perturbations of the Wind Stress Field over the Southern Ocean on Seasonal Timescales. *J. Climate*, **16**, 2340 - 2354.
- Palmer, T.N., and Z. Sun, 1985: A modeling and observational study of the relationship between sea surface temperature in the north-west Atlantic and the atmospheric general circulation. *Q.J.R. Met. Soc.*, **111**, 947 - 975.
- Peng, S., L.A. Mysak, H. Ritchie, J. Derome, and B. Dugas, 1995: The Differences between Early and Midwinter Atmospheric Responses to Sea Surface Temperature Anomalies in the Northwest Atlantic. *J. Climate*, **8**, 137 - 157.

- Quadrelli, R., and J.M. Wallace, 2004: A Simplified Linear Framework for Interpreting Patterns of Northern Hemisphere Wintertime Climate Variability. *J. Climate*, **17**, 3728 - 3744.
- Rodwell, M.J., and C.K. Folland, 2002: Atlantic air-sea interaction and seasonal predictability. *Q.J.R. Meteorol. Soc.*, **128**, 1413 - 1443.
- Sampe, T., H. Nakamura, A. Goto, and W. Ohfuchi, 2010: Significance of a Midlatitude SST Frontal Zone in the Formation of a Storm Track and an Eddy-Driven Westerly Jet. *J. Climate*, **23**, 1793 - 1814.
- Santer, B.D, T.M.L. Wigley, J.S. Boyle, D.J. Gaffen, J.J. Hnilo, D. Nychka, D.E. Parker, and K.E. Taylor, 2000: Statistical significance of trends and trend differences in layer-average atmospheric temperature time series. *J. Geophys. Res.*, **105**, 7337 - 7356.
- Smirnov, D., M. Newman, and M.A. Alexander, 2014a: Investigating the Role of Ocean-Atmosphere Coupling in the North Pacific Ocean. *J. Climate*, **27**, 592 - 606.
- Smirnov, D., M. Newman, M.A. Alexander, Y-O. Kwon, and C. Frankignoul, 2014b: Investigating the Local Atmospheric Response to a Realistic Shift in the Oyashio Sea Surface Temperature Front. *J. Climate*, **28**, 1126 - 1147.
- Visbeck, M., Chassignet, E. P., Curry, R. G., Delworth, T. L., Dickson, R. R. and Krahnemann, G., 2003: The Ocean's Response to North Atlantic Oscillation Variability, in *The North Atlantic Oscillation: Climatic Significance and Environmental Impact* (eds J. W. Hurrell, Y. Kushnir, G. Ottersen and M. Visbeck), American Geophysical Union, Washington, D. C.. doi: 10.1029/134GM06
- Walker, G.T., and E.W. Bliss, 1932: World weather V. *Mem. Roy. Meteor. Soc.*, **4**, 53 - 84.

Wallace, J.M., and D.S. Gutzler, 1980: Teleconnection in the Geopotential Height Field during the Northern Hemisphere Winter. *Mon. Wea. Rev.*, **109**, 784 - 812.

Wallace, J.M., C. Smith, and Q. Jiang, 1990: Spatial Patterns of Atmosphere-Ocean Interaction in the Northern Winter. *J. Climate*, **3**, 990 - 998.

Wallace, J.M., and D.W.J. Thompson, 2002: The Pacific Center of Action of the Northern Hemisphere Annular Mode: Real or Artifact?. *J. Climate*, **15**, 1987 - 1991.